The spectral energy distribution of powerful starburst galaxies – I. Modelling the radio continuum

T. J. Galvin,[1,2,3]★ N. Seymour,[2]★ J. Marvil,[3] M. D. Filipović,[1] N. F. H. Tothill,[1]
R. M. McDermid,[4,5] N. Hurley-Walker,[2] P. J. Hancock,[2,6] J. R. Callingham,[3,6,7]
R. H. Cook,[2,8] R. P. Norris,[1,3] M. E. Bell,[3,6] K. S. Dwarakanath,[9] B. For,[8]
B. M. Gaensler,[6,7,10] L. Hindson,[11] M. Johnston-Hollitt,[11,12] A. D. Kapińska,[6,8]
E. Lenc,[6,7] B. McKinley,[6,13] J. Morgan,[2] A. R. Offringa,[6,14] P. Procopio,[6,15]
L. Staveley-Smith,[6,8] R. B. Wayth,[2,6] C. Wu[8] and Q. Zheng[11]

Affiliations are listed at the end of the paper

ABSTRACT

We have acquired radio-continuum data between 70 MHz and 48 GHz for a sample of 19 southern starburst galaxies at moderate redshifts ($0.067 < z < 0.227$) with the aim of separating synchrotron and free–free emission components. Using a Bayesian framework, we find the radio continuum is rarely characterized well by a single power law, instead often exhibiting low-frequency turnovers below 500 MHz, steepening at mid to high frequencies, and a flattening at high frequencies where free–free emission begins to dominate over the synchrotron emission. These higher order curvature components may be attributed to free–free absorption across multiple regions of star formation with varying optical depths. The decomposed synchrotron and free–free emission components in our sample of galaxies form strong correlations with the total-infrared bolometric luminosities. Finally, we find that without accounting for free–free absorption with turnovers between 90 and 500 MHz the radio continuum at low frequency ($\nu < 200$ MHz) could be overestimated by upwards of a factor of 12 if a simple power-law extrapolation is used from higher frequencies. The mean synchrotron spectral index of our sample is constrained to be $\alpha = -1.06$, which is steeper than the canonical value of -0.8 for normal galaxies. We suggest this may be caused by an intrinsically steeper cosmic ray distribution.

Key words: galaxies: starburst – radio continuum: galaxies.

1 INTRODUCTION

Understanding the star formation history of the Universe is one of the key science goals of the Square Kilometre Array (SKA; Prandoni & Seymour 2015) and its pathfinder projects (Norris et al. 2011). Radio-continuum emission offers a unique advantage over other wavebands, as it is impervious to the effects of dust attenuation and is able to provide an unbiased view into the star formation rates (SFRs) of distant galaxies through cosmic time (Seymour et al. 2008; Jarvis et al. 2015). Current critical radio-continuum SFR indicators, based mostly on the 1.4 GHz luminosity, have been calibrated against far-infrared (FIR) measures using the FIR-to-radio correlation (FRC; Condon 1992).

The FRC itself is a tight, linear relationship across many orders of magnitude between the FIR and radio-continuum luminosities of star-forming galaxies (SFGs; Yun, Reddy & Condon 2001; Bell 2003; Mao et al. 2011). Its existence is composed of three individual emission processes that are all manifestations of high-mass star (HMS; $M_\odot > 8\,M_\odot$) formation.

FIR emission, spanning 40–500 μm, originates from widespread dust cirrus heated by ultraviolet (UV) and optical emission from a combination of mostly young HMS and an older stellar population. The observed radio continuum is a superposition of two individual mechanisms, the most prominent at low frequencies being nonthermal synchrotron emission. This process is thought to be formed from the relativistic electrons, accelerated by the remnants of Type II and Type Ib supernova of HMS, gyrating within large-scale galactic magnetic fields. Although synchrotron emission makes up roughly 90 per cent of the radio continuum at 1.4 GHz of normal galaxies, it

★ E-mail: t.galvin@westernsydney.edu.au (TJG); nick.seymour@curtin.edu.au (NS)

is a delayed tracer to SF, taking upwards of 10^7 yr for the electrons to diffuse (Condon 1992).

Thermal free–free emission is the second mechanism that makes up the radio continuum. Its underlying process is powered by the ionization of H II regions by UV flux from HMSs. Unlike synchrotron emission, it is a direct, near instantaneous tracer of SFR. Despite this, it is relatively unused as a radio-continuum SFR indicator due to its flat spectral index ($\alpha = -0.1$, where $S \propto \nu^{\alpha}$) and the fact that at low frequencies, where the survey speeds of radio telescopes are most efficient, the spectrum is overwhelmingly dominated by synchrotron. Isolating it requires either model fitting using a broad, densely sampled radio-continuum spectral energy distribution (SED; Price & Duric 1992; Galvin et al. 2016), or high-frequency observations ($\nu > 20$ GHz) where synchrotron emission is mostly absent (Murphy et al. 2012).

Although calibrating the radio-continuum SFR measures through the FRC has proved effective in the local Universe ($z < 0.15$), there remains considerable uncertainty as to how their reliability will scale with increasing redshifts. Murphy (2009) argues that due to a combination of the changing composition of the radio continuum with increasing frequencies and the suppression of synchrotron emission due to inverse-Compton (IC) scatter off the cosmic microwave background, scaling is in proportion to $(1 + z)^4$, that there should be an evolution in the observed frame FRC. Observational evidence presented by both Ivison et al. (2010) and Mao et al. (2011) uses image stacking techniques to demonstrate no change in the FRC up to redshifts of 2, suggesting that the physical origin of the FRC may be more complex than first thought.

Future radio-continuum surveys expected from the SKA and its pathfinder projects will explore the high-redshift Universe ($z > 1.0$). In this parameter space, it is expected that distant, faint SFGs, whose SFRs are in excess of $100 \, M_{\odot} \, yr^{-1}$, will be the predominant class of object detected with these surveys. Work by Clemens et al. (2010) also shows that the effects of free–free absorption, particularly in the case of multiple star-forming regions with different optical depths, will further complicate the observed radio continuum. Although synchrotron self-absorption can produce turnover features that can complicate the observed SED, SFGs do not have the required brightness temperatures (Condon 1992). Correctly interpreting the emission properties that trace star formation will require an improved understanding of the underlying physical mechanisms and how they can be characterized through their diverse SEDs.

In this study, we investigate the intrinsic emission components of 19 powerful star-forming luminous infrared galaxies (LIRGs), which are ideal representative sources of distant SFGs, at redshifts between 0.0627 and 0.227. We construct a series of comprehensive radio-continuum SEDs, ranging between 70 MHz and 48 GHz in the observed frame with the aim of isolating the thermal free–free component and identifying the effects of free–free absorption (FFA) at low frequency. As the free–free emission (1) is a direct tracer of SFR, (2) exhibits a flat spectral slope and (3) originates from the same H II regions as hydrogen recombination lines, it is an excellent candidate to craft SFR measures that are compatible with the high-redshift SFGs that will be revealed with SKA and its pathfinder projects. For our sample of objects, we have also acquired optical spectroscopy data using the Wide-Field Spectrograph (Dopita et al. 2007, 2010). We will analyse the optical spectroscopic data in conjunction with this radio-continuum modelling in a subsequent series of papers.

We assume a flat Universe, where $\Omega_m = 0.277$, $\Omega_{\lambda} = 0.733$ and $H_0 = 70.2 \, km \, s^{-1} \, Mpc^{-1}$ following Komatsu et al. (2009).

Table 1. The complete source sample used throughout this study. *IRAS* F14378-3651 was ultimately excluded from further processing due to LST constraints.

Name *IRAS*	RA J2000	Dec. J2000	z	$L_{8-1000 \, \mu m}$ $Log \, L_{\odot}$
F00198-7926	00:21:53.6	−79:10:07.79	0.07	12.12
F00199-7426	00:22:07.0	−74:09:41.89	0.10	12.22
F01268-5436	01:28:47.7	−54:21:25.62	0.09	11.97
F01388-4618	01:40:55.9	−46:02:53.32	0.09	12.08
F01419-6826	01:43:17.1	−68:11:24.12	0.08	11.8
F02364-4751	02:38:13.9	−47:38:11.34	0.10	12.05
F03068-5346	03:08:20.9	−53:35:17.66	0.07	11.9
F03481-4012	03:49:53.8	−40:03:41.03	0.10	11.86
F04063-3236	04:08:18.9	−32:28:30.35	0.11	12.07
F06021-4509	06:03:33.6	−45:09:41.12	0.16	12.23
F06035-7102	06:02:54.1	−71:03:10.48	0.08	12.15
F06206-6315	06:21:01.2	−63:17:23.81	0.09	12.2
F14378-3651	14:40:59.0	−37:04:32.24	0.07	12.07
F18582-5558	19:02:24.0	−55:54:08.56	0.07	11.63
F20117-3249	20:14:55.3	−32:40:00.50	0.10	11.92
F20445-6218	20:48:44.1	−62:07:25.35	0.11	11.95
F21178-6349	21:21:53.8	−63:36:43.68	0.07	11.63
F21292-4953	21:32:36.2	−49:40:24.74	0.14	12.39
F21295-4634	21:32:49.4	−46:21:03.93	0.07	11.72
F23389-6139	23:41:43.5	−61:22:52.62	0.09	12.14

2 DATA

2.1 Source selection

In this study, we selected a sample of all known southern ($\delta < -30°$) LIRGs, defined as having IR luminosities greater than $L_{8-1000 \, \mu m} > 10^{11} \, L_{\odot}$. These objects were specifically targeted due to their high SFR, as this implies that there would be a measurable thermal component in their radio continuum. These types of objects are analogous to the types of distant SFGs that are expected to predominately comprise the next generation of future deep surveys.

The sample for this study was constructed using the Revised *IRAS* Faint Source Catalog (Wang et al. 2014). We identified all sources with a 60 μm flux density in excess of 1.4 Jy ($S_{60 \, \mu m} > 1.4$ Jy) and a spectroscopic redshift in the range of $0.067 < z < 0.227$. This was done not only to target galaxies with high SFR but also to allow for future ground-based observations of the Paschen-α (Paα; $\lambda = 1.875 \, \mu m$) hydrogen recombination line, which is a relatively un-attenuated measure of star formation. Potential sources were cross-referenced with the Sydney University Molonglo Sky Survey (SUMSS) catalogue (Mauch et al. 2003, 2013) in order to obtain radio flux densities at 843 MHz.

In order to construct a representative sample of SFGs, sources with a detectable active galactic nucleus (AGN) component, as seen in their optical spectra, or those flagged as a quasi-stellar objects by Wang et al. (2014), were excluded from further consideration. We also scaled the SUMSS flux density measurement to 1.4 GHz using the model described by Condon (1992) to assess potential AGN activity. Sources defined as radio or infrared excess (five times as much radio or infrared luminosities expected when considering the FRC) following Yun et al. (2001) were also discarded, as such excess is indicative of the presence of AGN (see the q parameter defined below). After excluding sources with some AGN indicator, our final sample consisted of 20 sources. We list their positions, spectroscopic redshifts and IR luminosities in Table 1.

Table 2. An overview of the ATCA data (Project code: C2993, PI: Galvin) obtained as part of this study. All data used the compact array broad-band backend, giving a total of 2.048 GHz per central frequency. We include the Largest Angular Scale (LAS) that each array is sensitive to.

Central frequency (GHz)	Band	Array	Date observed	LAS (arcsec)
2.1	*L/S*	6A	23-01-2015	89.0
5.0	*C/X*	6A	27-01-2015	37.4
5.0	*C/X*	750C	29-12-2015	275.3
6.8	*C/X*	6A	27-01-2015	27.5
6.8	*C/X*	750C	29-12-2015	201.7
8.8	*C/X*	6A	27-01-2015	21.2
8.8	*C/X*	750C	29-12-2015	155.9
10.8	*C/X*	6A	27-01-2015	17.31
10.8	*C/X*	750C	29-12-2015	127.0
17.0	*K*	6A	23-01-2015	11.0
17.0	*K*	750C	31-12-2015	80.9
17.0	*K*	H168	06-09-2016	60.5
21.0	*K*	6A	23-01-2015	8.9
21.0	*K*	750C	31-12-2015	65.3
21.0	*K*	H168	06-09-2016	49.0
45.0	*Q*	H214	4-09-2014	17.0
47.0	*Q*	H214	4-09-2014	15.9
89.0	*W*	H214	4-09-2014	8.6
93.0	*W*	H214	4-09-2014	8.2

2.2 Australia Telescope Compact Array observations

Over five nonconsecutive nights, 19 of the 20 sources in our sample (*IRAS* F14378-3651 was dropped due to LST constraints) were observed across 11 central frequencies (Table 2) using the Australia Telescope Compact Array (ATCA; Frater, Brooks & Whiteoak 1992; Wilson et al. 2011) under the project code C2993 (PI: Galvin). With the Compact Array Broad-band Backend (CABB) filters, a spectral window of 2.048 GHz was available for each of the targeted central frequencies. In total, this provided roughly 22.5 GHz of coverage from 1.1 to 94.0 GHz. We adopted a snapshot imaging approach due to the diverse LST range of our sample. To help optimize efficiency, we grouped sources based on their positions to share phase reference calibrators. This was important as at high frequencies an increasingly large fraction of time is lost to calibration overheads (i.e. pointing calibrations and phase reference scans).

The first night on 2014 October 4 targeted the *Q*- and *W*-band frequencies and was performed in a H214 hybrid configuration. This compact array configuration was selected to help prevent resolving out source structure. PKS 1921−293 (RA, Dec. J2000: 19:24:51.05, −29:14:30.12) was used as the bandpass calibrator, while Uranus was used to provide a flux density scale. Due to the high frequency, pointing calibrations were performed between each slew greater than 10°. A full hour angle synthesis was not possible due to the considerable overheads required with observing at these frequencies. Instead, we elected to observe each source for a single 15 min exposure and measure the flux of each source in the (*u*, *v*)-plane exclusively. Although normally a single cut in the (*u*, *v*)-plane would introduce source confusion, the H214 hybrid array, with two antenna along the north–south spur, provided enough spatial coverage to sample the (*u*, *v*)-plane adequately enough to isolate our sources in the sky. Elevated path noise (a measure of the atmospheric phase stability; Middelberg, Sault & Kesteven 2006) only allowed us to observe six sources at the *W*-band central frequencies. Ultimately,

these *W*-band data were discarded due to difficulties during calibration.

Centimetre data were collected over a number of individual observing runs. Initially, *L*- and *K*-band data were collected on 2015 January 23 in a 6A array configuration. We used PKS 1934-638 to provide a flux density calibration for both bands. For *K*-band data taken on this night, PKS 1921-293 was used as a bandpass calibrator. During this initial 12 h observing run, each source was observed for at least 5 min across at least three cuts. A phase calibrator was also visited at least once every 10 min. Subsequent *K*-band data were collected on 2015 December 30 and 2016 September 26 in compact 750C and H168 array configurations. Data obtained in the 750C array configuration used the same observing strategy outlined above. For the H168 array *K*-band observing, we elected to dwell on each source for a single 10 min block of time across a single 4 h block of unallocated telescope time. This 'single block' approach minimized the total time lost to overheads, while, with the addition of the north–south spur, adequately sampled the innermost (*u*, *v*)-region. A phase reference scan was made after each source.

The *C/X*-band frequencies were obtained across two separate observing runs totalling roughly 17 h. The first, performed on 2015 January 27 for 12 h, used a sparsely distributed 6A configuration. On 2015 December 29, we again revisited the sample in a compact 750C array. For both observing sessions, PKS 1934-638 was used as a bandpass calibrator and flux density scale. In total, across both observing runs each source was observed for roughly 7 min across at least four cuts.

Due to the wide range of LST of our sources, we were not able to ensure a consistent amount of integration time equally spread across the (*u*, *v*)-space for our complete sample. Traditionally, this would be a problem for image deconvolution due to the poorly constrained instrumental response, but as we are primarily interested in a known source at the phase centre of each pointing, this is not a critical issue. Hence, our major obstacle is trying to prevent resolving source structure with increasing resolution. The inclusion of a short baseline data from 750C, H214 and H168 array configurations for the *C/X* and *K* bands and a natural weighting scheme helped in this regard. Collectively, the combination of data was sensitive to roughly the same angular scales.

2.3 Murchison Widefield Array

Low-frequency data were obtained from the SKA-LOW precursor, the Murchison Widefield Array (MWA; Lonsdale et al. 2009; Tingay et al. 2013). Located in Western Australia, it is composed of 2048 dual polarization dipole antennas capable of operating between 70 and 320 MHz with an instantaneous frequency coverage of 30.72 MHz.

One of its key science products, entitled the GaLactic and Extragalactic MWA Survey (GLEAM; Wayth et al. 2015), is imaging the low-frequency sky for declinations south of +30 deg. The survey itself covers 30 000 deg^2 to an ≈90 per cent completeness level at 160 mJy. A description of the observing, calibration, imaging and post-image calibration strategies to extract an extragalactic source catalogue is presented by Hurley-Walker et al. (2017). GLEAM is the largest fractional bandwidth all-sky survey to date, with the final catalogue containing 20 sub-band flux density measurements for each source across most of the MWA frequency range. The internal flux calibration is better than 3 per cent and is based on the Baars et al. (1977) scale.

Source identification and extraction in GLEAM (as outlined by Hurley-Walker et al. 2017) were performed using the AEGEAN

software package (Hancock et al. 2012). A deep image covering the frequency range of 170–231 MHz was used to extract an initial reference catalogue. After applying quality control measures, the flux density of each source in this reference catalogue was then measured in the twenty 7.68 MHz narrow-band images that span the 72–231 MHz frequency range (Hurley-Walker et al. 2017).

2.3.1 Detected sources

We inspected the GLEAM catalogue to obtain possible low-frequency flux densities for our sample of galaxies. Owing to the resolution of GLEAM, which is around 120 arcsec, we compared potential matches by eye[1] to ensure that they were genuine detections in a non-confused field. We found sources *IRAS* F00198-7926, *IRAS* F01268-5436, *IRAS* F02364-4751, *IRAS* F03068-5346, *IRAS* F03481-4012, *IRAS* F04063-3236, *IRAS* F21292-4953 and *IRAS* F23389-6139 had clear counterparts in the catalogue. Source *IRAS* F06035-7102, being in the direction of the Large Magellanic Cloud (LMC), was not included in this release of GLEAM. Subsequent source extraction for this source was carried out for a small region surrounding it using the GLEAM pipeline. Some sub-band measurements were discarded, as they were described as having negative integrated flux densities. This was possible as the sensitive 170–231 MHz reference image was used to identify sources, whose positions was fixed when the same sources were fitted in the noisier sub-band images.

2.3.2 Non-detections

For sources in our sample without a reliable MWA detection, we used the PRIORIZED option available in AEGEAN to estimate the flux density and uncertainty in the GLEAM broad-band images. These broad-band images were at central frequencies of 88, 115, 155, each with 30 MHz of frequency coverage, and 200 MHz with 60 MHz of bandwidth. PRIORIZED allows the user to fix properties of some source (including its position) and specify characteristics of the MWA synthesized beam while fitting for an object. Using this method, we were able to obtain a further set of low significance measurements for sources *IRAS* F00199-7426, *IRAS* F01388-4618, *IRAS* F01419-6826, *IRAS* F06021-4509, *IRAS* F06206-6315, *IRAS* F18582-5558, *IRAS* F20117-3249, *IRAS* F20445-6218, *IRAS* F21178-6349 and *IRAS* F21295-4634.

All MWA GLEAM measurements described in Sections 2.3.1 and 2.3.2 are listed in Table A1.

2.4 Archived radio-continuum data

The Australian Telescope Online Archive[2] (ATOA) was used to search for existing ATCA data of sources in our sample. Projects C222 and C593 were found to have observed *IRAS* F00199-7426 and *IRAS* F23389-6139, respectively. Their bandwidth was limited to 128 MHz, as they were taken using the pre-CABB ATCA correlator. We summarize these observations in Table 3.

Table 3. An overview of the archival ATCA data identified for this project. All observations used the pre-CABB ATCA correlator, providing only 128 MHz of bandwidth.

Project	Date	ν (GHz)	RA (J2000)	Dec. (J2000)
C222	21-6-1993	4.8	00:22:08.4	−74:08:31.95
	21-6-1993	8.6	00:22:08.4	−74:08:31.95
C539	5/7-1-1998	4.8	22:39:09.4	−82:44:11.00
	5/7-1-1998	8.6	22:39:09.4	−82:44:11.00
	27/28-1-1998	4.8	22:39:09.4	−82:44:11.00
	27/28-1-1998	8.6	22:39:09.4	−82:44:11.00
	27-1-2002	1.4	22:39:09.4	−82:44:11.00
	27-1-2002	2.5	22:39:09.4	−82:44:11.00

2.5 Other data

We sourced any radio continuum or FIR flux density measurements from the literature for each of our sources. Initially, we collected measurements from the photometry tables for our sample tracked by the online NED[3] tool.

Additional FIR measurements were obtained from the *AKARI* space telescope (Murakami et al. 2007). With the exception of *IRAS* F21295-4634 and *IRAS* F23389-6139, all sources in our sample were detected at 90 μm in the *AKARI* All-Sky Survey Point Source Catalog (Yamamura et al. 2010). Brighter sources were also detected at 65 and 140 μm. These measurements were not included in the photometry tables retrieved from NED. We list all measurements that we obtained from either NED, with references to their origin, or Yamamura et al. (2010) in Table A2.

An image of the LMC at 20 cm presented by Hughes et al. (2006, 2007) was used to obtain a single flux density measurement at 1.4 GHz for *IRAS* F06035-7102. This was particularly important, as our *L/S*-band ATCA data for this source was difficult to image, and ultimately discarded, due to its sparse (u, v)-sampling and the complexity of the LMC field.

3 DATA REDUCTION

3.1 ATCA radio continuum

The MIRIAD (Sault, Teuben & Wright 1995) and KARMA (Gooch 1996) software packages were used for data reduction and analysis of the ATCA data. The guided automated flagging MIRIAD routine PGFLAG was used in conjunction with more traditional MIRIAD flagging and calibration tasks in order to perform an initial data reduction. Given the wide bandwidth of the CABB system, appropriate MIRIAD tasks used the NFBIN option to derive a frequency-dependent calibration solution.

Once a calibration solution was applied to each of the observation programme sources, the centimetre data were then imaged individually across all frequency bands using their complete bandwidth ($\Delta\nu = 2.048$ GHz, minus the edge channels automatically flagged by ATLOD). A Briggs robust parameter value of 2, corresponding to natural weighting, was used to provide the maximum signal-to-noise ratio (SNR) at the cost of producing a larger synthesized beam. Given the large fractional bandwidth provided by CABB, MFCLEAN (Sault & Wieringa 1994) was used to deconvolve the multifrequency synthesized dirty map. MIRIAD tasks RESTOR and

---

[1] Using the GLEAM postage stamp server found at http://mwa-web.icrar.org/gleam_postage/q/form.
[2] http://atoa.atnf.csiro.au/

[3] http://ned.ipac.caltech.edu/

LINMOS were used in conjunction to deconvolve sidelobe artefacts and performed primary beam correction while accounting for the spectral index of the clean components. These preliminary images were produced in order to inspect and compare the applied calibration solution amongst the *uv* data sets for each source.

An iterative procedure, similar to that used by Galvin et al. (2016), was used to exploit the generous 2 GHz of bandwidth provided by the ATCA CABB system. Initially, each CABB band was imaged individually using the recipe outlined above. Next, the MIRIAD task IMFIT was used to constrain each source of interest using a single-point source model. If the extracted peak flux density was above an SNR of 8 then the CABB data set would be split into an increasing number of sub-bands and reprocessed. We also ensured that each sub-band had a fraction bandwidth larger than 10 per cent so that MFCLEAN could safely be used. Given sufficient SNR across all sub-bands, this iterative procedure would continue to a maximum of four sub-bands. We utilized the LINE parameter in INVERT to ensure that each image shared an equal amount of un-flagged channels. With such an approach, sources with high SNR were split into multiple data points, which could be used to better constrain the radio-continuum emission models (see Section 4.2).

For high-frequency *Q*- and *W*-band observations, we used the MIRIAD task UVFIT to fit a single-point source model directly to the (*u*, *v*) data for each source. We elected not to iteratively increase the number of sub-bands (similar to the process outlined above) or include a spectral index as a parameter while fitting to the visibilities (implemented in the MIRIAD task UVSFIT) as at these frequencies, where the fractional bandwidth is below 5 per cent and spectral variation would be difficult to constrain.

For archived data, where only 128 MHz of data were available, the NFBIN option was not used during typical calibration procedures.[4] A joint deconvolution method was applied to applicable data sets, namely those from C539, to minimize the resulting noise characteristics. Otherwise normal imaging procedures were used to deconvolve the beam response and apply primary beam corrections to all images. The task IMFIT was used to fit a point source model to sources of interest. Image residuals were inspected to ensure an adequate fit.

3.1.1 Resolving structure

We examined the outputs of the iterative imaging process, including the modelled point source residuals, SUMSS images and the initial SEDs that the imaging pipeline produced to assess whether our data were resolving components of an object. This review showed that our 4 cm data for *IRAS* F06035-7102 were detecting extended structure distinct from the main component of the source and within the SUMSS source. Therefore, we applied a convolving beam of 45 × 45 arcsec (the same size of the SUMSS restoring beam) to all images above a frequency of 4 GHz for this source, which was used to extract peak flux densities from. We added an additional 10 per cent error in quadrature for these measurements.

To assess whether there were other sources in our sample with similar diffuse features, we compared the peak fluxes obtained by fitting a point source model to all images before and after they were convolved with a 45 × 45 arcsec Gaussian kernel, as well as the integrated flux of a Gaussian model fitted to the non-convolved image. We found that there was weak evidence of structure for *IRAS* F21292-4953 above frequencies of 6 GHz. Convolved peak

flux density measurements were therefore used for images between $4.0 < \nu < 22.0$ for this source. Otherwise, there were no other sources showing flux densities that were inconsistent amongst these methods.

IRAS F23389-6139, however, showed that the 4 cm *C/X* bands were roughly ∼6 mJy below the ATCA pre-CABB fluxes from project C539 and the trend seen between 3 and 17 GHz. When investigating, we found that measurements made using the visibilities directly with the MIRIAD task UVFIT produced results that were in excellent agreement to the rest of the data. We believe that this difference in peak flux densities was the combination of clean bias and imaging artefacts that could not be deconvolved due to the sparse (*u*, *v*)-sampling.

Our typical restoring beams were 20 × 10 arcsec in *L* band, 10 × 5 arcsec in the *C/X* band and 5 × 3 arcsec in the *K* band. For each image, we also computed the brightness temperature sensitivity. We compared this to the model from Condon (1992) normalized to 1 K at 1.4 GHz, the median brightness temperature of a face on spiral galaxy (Condon et al. 1998). The brightness temperatures of our images were all higher than this lower limit.

All ATCA flux density measurements obtained under the project code C2993 are listed in Table A3.

4 SED MODELLING

4.1 Variability

Multi-epoch observations and source variability could give a false impression of curvature or complexity in an observed SED. For this study, the majority of our data were collected within a 2 yr time span. SFGs do not show variability on such time-scales at our sensitivities (Mooley et al. 2016). MWA GLEAM Data Release One (DR1) conducted its observing campaign between 2013 August and 2014 July. Over this time frame, multiple drift scans were performed across the southern sky before combining all available data into the final image set. Likewise, the majority of our ATCA data were taken between 2014 September and 2015 February, with selected frequency bands being observed in compact array configurations up to 2016 September.

4.2 Radio-continuum models

Given the broad coverage of our radio-continuum data, which covers 70 MHz to 48 GHz in the observed frame, and the size of our sample we elected to fit a series of increasingly complex models to all sources. All modelling was performed in the rest frame with a reference frequency, unless stated otherwise, of $\nu_0 = 1.4$ GHz.

4.2.1 Power law

Initially, we fit a simple power law (which we label as 'PL' in subsequent tables and figures) to all available flux density measurements, in the form of

$$S_\nu = A \left(\frac{\nu}{\nu_0} \right)^\alpha. \tag{1}$$

The terms *A* and the spectral index, α, are treated as free parameters and represent a normalization component and the gradient in logarithmic space.

4.2.2 Synchrotron and free–free emission

We can model the radio continuum as the sum of two distinct power laws. One representing the steep spectrum non-thermal synchrotron emission, and the second describing the flat spectral thermal free–free emission, following the form:

$$S_\nu = A \left(\frac{\nu}{\nu_0} \right)^\alpha + B \left(\frac{\nu}{\nu_0} \right)^{-0.1}, \qquad (2)$$

where A and B are treated as free parameters and represent the synchrotron and free–free normalization components, respectively. The free parameter α represents the synchrotron spectral index and, depending on the history of injected cosmic rays, is known to vary (Niklas, Klein & Wielebinski 1997). This model describes both synchrotron and free–free emission components as being completely optically thin (i.e. no curvature at low frequencies). We label this model as 'SFG NC'.

4.2.3 Synchrotron and free–free emission with free–free absorption

When synchrotron and free–free emission are in a coextensive environment, synchrotron emission can be attenuated by free–free absorption (FFA) processes producing a low-frequency turnover. This attenuation is influenced by the flux density, density and spatial distribution of the ionized free–free emission with respect to the non-thermal synchrotron emission. If the frequency of this turnover from free–free absorption is parametrized by $\nu_{t,1}$, then the optical depth can be described as $\tau = (\nu/\nu_{t,1})^{-2.1}$. Following Condon (1992) and Clemens et al. (2010), we describe this more complete model (labelled as 'C' throughout) as

$$S_\nu = \left(1 - e^{-\tau} \right) \left[B + A \left(\frac{\nu}{\nu_{t,1}} \right)^{0.1+\alpha} \right] \left(\frac{\nu}{\nu_{t,1}} \right)^2, \qquad (3)$$

where ν_t is the turnover frequency where the optical depth reaches unity and α is the spectral index of the synchrotron emission. A and B represent the synchrotron and free–free emission components. We fit for A, B, $\nu_{t,1}$ and α simultaneously. To minimize model degeneracy, particularly in the case when normalization components are subject to the ν^2 scaling in the optically thick regime, we replace the ν_0 term, set to 1.4 GHz in other models, to instead be the turnover frequency parameter for each component.

4.2.4 Multiple FFA components

Model 'C' assumes a single volume of thermal free–free plasma intermixed with synchrotron emission produced by relativistic electrons. Although this model was derived from observations of the irregular, clumpy galaxy Markarian 325 (Condon & Yin 1990), Clemens et al. (2010) present a set of LIRGs whose radio continuum show a number of high-frequency 'kinks' that could be attributed to multiple turnover features. Their interpretation suggests that when multiple star-forming regions with different compositions or geometric orientations are integrated over by a large synthesized beam, such is the case of an unresolved galaxy, the observed radio continuum could be complex.

Following this, we include an additional set of increasingly complex models that aim to capture these higher order features.

First, we assume a single relativistic electron population that produces the synchrotron emission, that is inhomogeneously mixed

with two distinct regions of star formation with distinct optical depths. This model (labelled 'C2 SA') may be described as

$$S_\nu = \left(1 - e^{-\tau_1} \right) \left[B + A \left(\frac{\nu}{\nu_{t,1}} \right)^{0.1+\alpha} \right] \left(\frac{\nu}{\nu_{t,1}} \right)^2$$
$$+ \left(1 - e^{-\tau_2} \right) \left[D + C \left(\frac{\nu}{\nu_{t,2}} \right)^{0.1+\alpha} \right] \left(\frac{\nu}{\nu_{t,2}} \right)^2, \qquad (4)$$

where τ_1 and τ_2 describe the optical depths of components 1 and 2 (each parametrized with their own turnover frequency $\nu_{t,1}$ and $\nu_{t,2}$), A and C are the normalization parameters for the synchrotron mechanism and B and D scale the free–free component. α is the spectral index of the single synchrotron population.

To account for sources where the low-frequency SED does not indicate a turnover due to FFA, we construct a model similar to 'C2 1SA' in the form of

$$S_\nu = \left(\frac{\nu}{\nu_0} \right)^{-2.1} \left[B + A \left(\frac{\nu}{\nu_0} \right)^{0.1+\alpha} \right] \left(\frac{\nu}{\nu_0} \right)^2$$
$$+ \left(1 - e^{-\tau_2} \right) \left[D + C \left(\frac{\nu}{\nu_{t,2}} \right)^{0.1+\alpha} \right] \left(\frac{\nu}{\nu_{t,2}} \right)^2. \qquad (5)$$

The model and its parameters, with the exception of τ_1 that has been removed, behave in the same way as 'C2 1SA'. The reference frequency for the low-frequency component is parametrized as ν_0 and set to 1.4 GHz. We maintain this form, as it allows the parameters A and B to be more directly comparable to C and D. We label this model as 'C2 1SAN'.

Next, we relax the single spectral index constraint. Although this introduces an additional parameter, its physical motivation is based on a galaxy merger, where two distinct systems merging drives a new burst of star formation. The electron distribution could, in such a scenario, be comprised of two different populations. We express this model as

$$S_\nu = \left(1 - e^{-\tau_1} \right) \left[B + A \left(\frac{\nu}{\nu_{t,1}} \right)^{0.1+\alpha} \right] \left(\frac{\nu}{\nu_{t,1}} \right)^2$$
$$+ \left(1 - e^{-\tau_2} \right) \left[D + C \left(\frac{\nu}{\nu_{t,2}} \right)^{0.1+\alpha_2} \right] \left(\frac{\nu}{\nu_{t,2}} \right)^2, \qquad (6)$$

where parameters carry the same meaning as in 'C2 SA' except we introduce parameters α and α_2 to characterize the synchrotron spectral indices of component 1 and component 2, respectively. We label this model simply as 'C2'.

4.3 FIR emission

For normal type galaxies heated dust, traced by FIR emission and approximated well by a grey body, begins to contribute a non-negligible fraction of the observed continuum at frequencies above 100 GHz (Condon 1992). A grey body is an optically thin, modified blackbody spectrum written as

$$S_\nu (\lambda) = I \times \left[\left(\frac{60 \, \mu m}{\lambda} \right)^{3+\beta} \times \frac{1}{e^{\frac{hc}{\lambda kT}} - 1} \right], \qquad (7)$$

where S_ν is the flux density in Jy at frequency ν, T is the absolute temperature of the body in kelvin, β represents the power-law variation of the emissivity with wavelength, and I is a normalization. The β component encodes properties of the distribution of dust

grains and their sizes with typical values in the range of 1–2 (Hildebrand 1983; Smith et al. 2013). To appropriately constrain these additional free parameters, we collect all measurements for each source up to $\lambda = 500\,\mu m$ available from the literature (summarized in Table A2).

For each radio-continuum model described in equations (1)–(6), we add a grey body component. The near orthogonal free–free and infrared emission components (specifically the Rayleigh–Jeans property of the grey body) allow us to reduce associated uncertainties for the thermal free–free emission while fitting each SED.

4.4 Fitting and selection

4.4.1 Model fitting

While fitting our SED models, we followed a similar fitting approach as described by Callingham et al. (2015). An 'affine invariant' Markov chain Monte Carlo ensemble sampler (Goodman & Weare 2010), implemented as the EMCEE[5] PYTHON package (Foreman-Mackey et al. 2013), was used to constrain each of described radio-continuum models for each source in our sample. This particular sampling method offers an efficient method of searching a parameter space, using a set of 'walkers', for regions of high likelihood during model optimization. These walkers are relatively insensitive to dependences or covariance amongst the free parameters being optimized. The samples these walkers draw from some parameter space can be marginalized over to estimate the probability density function of a set of parameters. In the Bayesian sense, this sampled space is referred to as the posterior distribution.

Assuming independent measurements whose errors are normally distributed, the log likelihood function that EMCEE attempts to maximize is expressed as

$$\ln \mathcal{L}(\theta) = -\frac{1}{2} \sum_n \left[\frac{(D_n - f(\theta))^2}{\sigma_n^2} + \ln\left(2\pi\sigma_n^2\right) \right], \qquad (8)$$

where D and σ are two vectors of length n containing a set of flux density measurements and their associated uncertainties, and $f(\theta)$ is the model to optimize using the parameter vector θ.

As stated in section 5.4 of Hurley-Walker et al. (2017), MWA GLEAM 7.68 MHz sub-band measurements have correlated errors, which violates an underlying assumption of equation (8). This covariance was introduced by a combination of their methods of applying primary beam, absolute flux scaling and ionosphere corrections and self-calibrating visibility data across 30.72 MHz before creating the final set of 20 sub-band images with 7.68 MHz widths. Some of these corrections have a direction-dependent component, meaning the degree of correlation amongst sub-bands can vary as a function of position. Although this could be accounted for with an appropriate covariance matrix, whose off-diagonal elements represent the degree of correlation for a pair of sub-band fluxes, at present such a matrix is not known. Without accounting for this, any inferences made from constrained models could be biased or incorrect.

We therefore adopted as part of our fitting routines a Matérn covariance function (Rasmussen & Williams 2006), which aims to model the off-diagonal elements of the unknown MWA GLEAM data covariance matrix. This is a radial-type covariance function that assumes that measurements closer together (for our problem closer together in frequency space) are more correlated that those

further apart. The form we adopt while performing all SED fitting is

$$k(r) = a^2 \left(1 + \frac{\sqrt{3}r}{\gamma} \right) \exp\left(-\frac{\sqrt{3}r}{\gamma} \right), \qquad (9)$$

where k is the parametrized Matérn covariance function, r is the $\Delta \nu$ between a pair of flux density measurements. a and γ are quantities constrained by EMCEE. The PYTHON module GEORGE[6] (Ambikasaran et al. 2015) was used to implement and manage the Matérn covariance function and supply the log likelihood, for only the GLEAM flux density measurements, of some model given θ. This was then summed with the log likelihood obtained using equation (8) for the independent flux density measurements and θ parameter vector. Note that the addition of a and γ increased the free parameters for each model by two. This covariance matrix modelling was not used for sources with a single MWA GLEAM flux density measurement.

4.4.2 Model priors

When constraining models within a Bayesian framework, 'priors' describe any known or likely conditions for each parameter in some θ set. Such priors can be as simple as limits to enforce a strict value range, or as complex as defining some distribution that the 'true' value of a parameter is likely to take. The sampled posterior that the walkers construct can be sensitive to the conditions encoded as parameter priors, particularly if complex prior distributions are used. Therefore, we use uniform priors that simply enforce a range of values some parameter is allowed to take. Uniform priors are also referred to as being 'uninformed' as no likely distribution has been supplied to the Bayesian fitting frameworks.

Throughout our model fitting, we ensure that normalization parameters A, B, C and D remain positive, that the spectral index parameters α and α_2 remain in the range of $-0.2 > \alpha > -1.8$, the turnover frequencies are between 10 MHz and 40 GHz, and the a and γ parameters of equation (9) are between -500 to 500 mJy and 1–200 MHz, respectively.

These priors are founded on the sound assumptions that flux densities are positive emission processes and we can only constrain turnovers within the range where we have data (note that some SEDs begin to flatten before the optical depth reaches unity). We construct the limits of the spectral index parameters α and α_2 to allow a diverse ranges of values in the literature (Condon & Yin 1990; Niklas et al. 1997; Clemens et al. 2010). For the Matérn covariance parameters a and γ, we make no assumption about their value and set their priors broad enough such that to encompass all GLEAM data.

4.4.3 Model selection

A Bayesian framework grants the ability to objectively test whether the introduction of additional model complexity (where additional complexity is not restricted to an increasing set of nested models) is justified by an improved fit that is not simply a symptom of overfitting. The evidence value, $\mathcal{Z}$, is defined as the integral of the complete parameter space. Although computationally difficult to numerically compute, especially in the case of increasing parameter dimensions, recent algorithms have proven to be adept at obtaining reliable estimates of its value. MULTINEST (Feroz, Hobson & Bridges 2009) uses a nested sampling method to obtain an estimate of the $\mathcal{Z}$ value.

---

[5] https://github.com/dfm/emcee

[6] https://github.com/dfm/george

Table 4. An overview of the natural log of the Bayes odds ratio from the MULTINEST fitting of each model to every source. For each source, the values presented below are the evidence values for each model divided by the most preferred model (i.e. model with highest evidence value). As the natural log of ratio is presented, the most preferred models have values in this table equal to $\log_e(1) = 0$ (bold-italic typeface). Less preferred models therefore have more negative numbers. Models where the ratio is less than $\log_e(3) = 1.1$ are considered indistinguishable from the most preferred model (italic typeface).

Source IRAS	PL	SFG NC	C	C2 1SAN	C2 1SA	C2
F00198-7926	−12.0	−13.2	−15.8	−10.4	*0.0*	*−0.9*
F00199-7426	−15.4	−17.0	−1.4	*0.0*	−1.9	−2.2
F01268-5436	−7.1	*0.0*	−2.2	−4.7	−5.1	−5.2
F01388-4618	−12.6	−14.3	*0.0*	−3.0	−3.7	−4.5
F01419-6826	*0.0*	−1.4	*−0.9*	−2.3	−2.9	−2.0
F02364-4751	−28.5	−30.1	*0.0*	−2.6	−2.4	−1.9
F03068-5346	−9.4	*−0.3*	*0.0*	*−0.9*	−2.6	−1.6
F03481-4012	*0.0*	−1.4	−3.5	−6.5	−3.8	−4.5
F04063-3236	−23.2	−24.8	−30.4	−9.5	*0.0*	−1.3
F06021-4509	−8.5	−10.2	−10.4	−1.8	*−0.0*	*0.0*
F06035-7102	−53.9	−55.1	−21.7	*0.0*	−1.7	−5.4
F06206-6315	−65.8	−67.2	−29.4	−23.1	*0.0*	*−0.3*
F18582-5558	−24.9	−26.5	−22.9	*−0.3*	*−1.1*	*0.0*
F20117-3249	−148.5	−150.0	−18.7	*0.0*	−7.5	−4.3
F20445-6218	−1.9	−3.3	*0.0*	−1.3	−3.3	−1.3
F21178-6349	−2.5	−3.2	*0.0*	−4.1	−1.6	−2.1
F21292-4953	*0.0*	−1.8	−4.3	−3.3	−5.9	−5.9
F21295-4634	−20.3	−21.9	*−0.1*	*0.0*	−2.0	*−1.0*
F23389-6139	−1451.1	−1452.6	−211.6	−146.5	*0.0*	*−1.1*

Given the $\mathcal{Z}$ values of competing models M_1 and M_2, one is able to determine whether a model is preferred over another given a set of data. The Bayes odds ratio between the evidence values $\mathcal{Z}_1$ and $\mathcal{Z}_2$ for models M_1 and M_2 is constructed as

$$\Delta\mathcal{Z} = e^{(\mathcal{Z}_1 - \mathcal{Z}_2)}. \tag{10}$$

The evidence supporting M_1 over M_2 is considered 'very strong' with a $\Delta\mathcal{Z}$ in excess of 150. If $\Delta\mathcal{Z}$ is between $150 > \Delta\mathcal{Z} > 20$ or $20 > \Delta\mathcal{Z} > 3$, then it is seen as either 'strong' or 'positive' evidence (respectively) supporting M_1 over M_2. When $\Delta\mathcal{Z}$ is less than 3, then M_1 and M_2 are indistinguishable from one another. This scale was established by Kass & Raftery (1995) and is considered the standard ladder for preferred model selection.

We summarize the results of the Bayes odds ratio test for all models in Table 4 and highlight the most preferred model with any of its competitors. While estimating $\mathcal{Z}$ for each model, MULTINEST was configured to search the same parameter space as EMCEE.
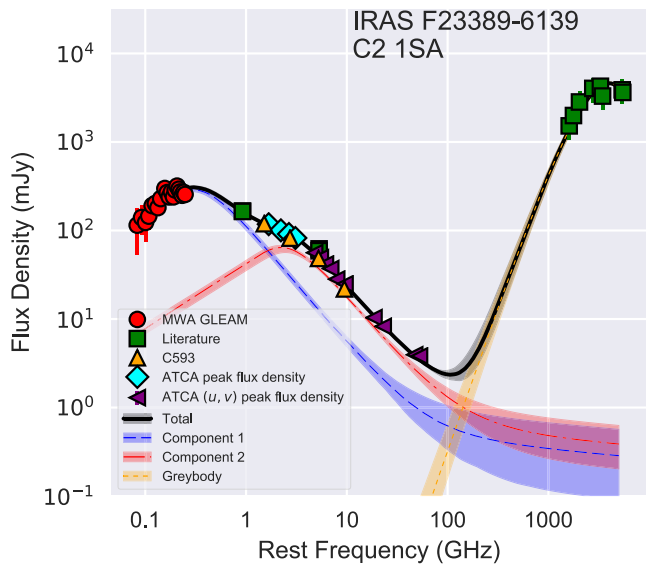
5 RESULTS

5.1 Model results

Nominal model parameters and their one sigma uncertainties, taken from the posterior distribution constructed by EMCEE, are shown in Table 5. Using the sampled posterior distribution, we take the 50th percentile as the nominal value, and the 16th and 84th represent the one sigma uncertainties. These posterior distributions were also saved and used when estimating derived quantities, including luminosities or thermal fractions, to accurately propagate errors and maintain covariance amongst given models fitted parameters.

An example of a final SED is presented in Fig. 1, with the remainder presented in the Appendix B. These SEDs include the most

Table 5. An overview of the most preferred models judged strictly by their evidence value and their constrained values. We use the 50th percentile of the samples posterior distribution as the nominal value, and use the 16th and 84th percentiles to provide the 1σ uncertainties. Parameters not included in a model are marked by a '–'. We omit parameters constrained that belong to the Matérn covariance function.

Source IRAS	Model	A (mJy)	B (mJy)	α	$\nu_{t,1}$ (GHz)	C (mJy)	D (mJy)	α_2	$\nu_{t,2}$ (GHz)	I (Jy)	Temp. K	β
F00198-7926	C2 1SA	$187.9^{+16.7}_{-15.2}$	$0.5^{+0.6}_{-0.4}$	$-1.3^{+0.1}_{-0.1}$	$0.2^{+0.0}_{-0.0}$	$7.6^{+0.8}_{-1.0}$	$0.5^{+0.4}_{-0.3}$	−	$6.2^{+0.7}_{-0.6}$	$0.23^{+0.06}_{-0.06}$	$55.5^{+4.5}_{-3.2}$	$1.3^{+0.3}_{-0.2}$
F00199-7426	C2 1SAN	$6.4^{+2.6}_{-3.0}$	$0.2^{+0.3}_{-0.2}$	$-0.8^{+0.0}_{-0.0}$	−	$46.6^{+21.8}_{-13.7}$	$0.2^{+0.3}_{-0.2}$	−	$0.5^{+0.2}_{-0.1}$	$1.52^{+0.41}_{-0.29}$	$40.1^{+1.8}_{-1.9}$	$1.1^{+0.2}_{-0.1}$
F01268-5436	SFG NC	$0.8^{+0.2}_{-0.2}$	$12.4^{+2.6}_{-0.4}$	$-1.0^{+0.0}_{-0.0}$	−	−	−	−	−	$0.34^{+0.22}_{-0.12}$	$44.7^{+4.6}_{-4.4}$	$1.3^{+0.4}_{-0.3}$
F01388-4618	C	$44.4^{+5.5}_{-4.2}$	$0.2^{+0.2}_{-0.1}$	$-0.7^{+0.0}_{-0.0}$	$0.3^{+0.0}_{-0.0}$	−	−	−	−	$0.59^{+0.25}_{-0.19}$	$45.7^{+3.8}_{-3.1}$	$1.6^{+0.2}_{-0.3}$
F01419-6826	PL	$8.7^{+0.3}_{-0.3}$	−	$-0.7^{+0.0}_{-0.0}$	−	−	−	−	−	$0.82^{+0.37}_{-0.32}$	$41.2^{+3.7}_{-2.5}$	$1.7^{+0.2}_{-0.4}$
F02364-4751	C	$86.5^{+4.7}_{-4.6}$	$0.3^{+0.3}_{-0.2}$	$-0.8^{+0.0}_{-0.0}$	$0.3^{+0.0}_{-0.0}$	−	−	−	−	$1.04^{+0.43}_{-0.30}$	$40.8^{+2.9}_{-2.4}$	$1.3^{+0.3}_{-0.2}$
F03068-5346	C	$147.1^{+205.1}_{-19.3}$	$2.5^{+0.4}_{-0.5}$	$-0.9^{+0.1}_{-0.1}$	$0.1^{+0.0}_{-0.1}$	−	−	−	−	$0.40^{+0.16}_{-0.08}$	$49.7^{+3.0}_{-3.4}$	$1.2^{+0.2}_{-0.1}$
F03481-4012	PL	$15.0^{+0.3}_{-0.4}$	−	$-0.8^{+0.0}_{-0.0}$	−	−	−	−	−	$0.29^{+0.12}_{-0.09}$	$47.3^{+3.8}_{-3.0}$	$1.5^{+0.3}_{-0.3}$
F04063-3236	C2 1SA	$49.4^{+4.4}_{-4.0}$	$0.2^{+0.3}_{-0.1}$	$-1.3^{+0.1}_{-0.1}$	$0.3^{+0.0}_{-0.1}$	$5.2^{+0.4}_{-0.4}$	$0.2^{+0.2}_{-0.1}$	−	$6.5^{+0.6}_{-0.7}$	$0.25^{+0.11}_{-0.08}$	$49.5^{+4.2}_{-3.7}$	$1.3^{+0.3}_{-0.3}$
F06021-4509	C2	$25.8^{+8.9}_{-8.8}$	$0.4^{+0.4}_{-0.4}$	$-1.1^{+0.2}_{-0.2}$	$0.4^{+0.3}_{-0.1}$	$5.0^{+1.2}_{-1.0}$	$0.4^{+0.3}_{-0.3}$	$-1.3^{+0.1}_{-0.1}$	$4.4^{+0.9}_{-0.7}$	$0.09^{+0.01}_{-0.01}$	$59.8^{+1.6}_{-1.8}$	$1.1^{+0.2}_{-0.2}$
F06035-7102	C2 1SAN	$23.2^{+3.6}_{-2.7}$	$0.3^{+0.4}_{-0.2}$	$-1.2^{+0.0}_{-0.0}$	−	$349.8^{+42.2}_{-38.6}$	$0.3^{+0.4}_{-0.3}$	−	$0.4^{+0.0}_{-0.0}$	$0.65^{+0.12}_{-0.11}$	$49.3^{+2.1}_{-1.7}$	$1.1^{+0.1}_{-0.0}$
F06206-6315	C2 1SA	$49.0^{+7.4}_{-8.4}$	$0.6^{+0.6}_{-0.4}$	$-1.3^{+0.1}_{-0.1}$	$0.5^{+0.1}_{-0.1}$	$12.8^{+0.9}_{-1.1}$	$0.5^{+0.4}_{-0.4}$	−	$4.5^{+0.4}_{-0.4}$	$0.67^{+0.13}_{-0.10}$	$45.9^{+1.8}_{-1.8}$	$1.1^{+0.1}_{-0.1}$
F18582-5558	C2	$213.2^{+191.4}_{-85.6}$	$0.3^{+0.4}_{-0.2}$	$-0.9^{+0.1}_{-0.1}$	$0.0^{+0.0}_{-0.0}$	$5.9^{+1.0}_{-0.9}$	$0.1^{+0.1}_{-0.1}$	$-1.3^{+0.2}_{-0.1}$	$5.4^{+0.7}_{-0.9}$	$0.48^{+0.07}_{-0.04}$	$43.4^{+1.5}_{-1.4}$	$1.8^{+0.1}_{-0.2}$
F20117-3249	C2 1SAN	$7.3^{+1.7}_{-1.3}$	$0.6^{+0.6}_{-0.4}$	$-1.1^{+0.1}_{-0.1}$	−	$73.0^{+3.4}_{-2.9}$	$0.5^{+0.6}_{-0.4}$	−	$1.6^{+0.2}_{-0.2}$	$1.14^{+0.57}_{-0.38}$	$37.1^{+2.5}_{-2.1}$	$1.7^{+0.2}_{-0.3}$
F20445-6218	C	$62.0^{+106.3}_{-15.7}$	$0.6^{+0.5}_{-0.4}$	$-0.8^{+0.1}_{-0.1}$	$0.2^{+0.1}_{-0.2}$	−	−	−	−	$0.40^{+0.24}_{-0.10}$	$46.6^{+3.1}_{-3.9}$	$1.3^{+0.3}_{-0.2}$
F21178-6349	C	$28.6^{+9.1}_{-7.0}$	$0.9^{+0.2}_{-0.2}$	$-1.2^{+0.1}_{-0.1}$	$0.4^{+0.1}_{-0.1}$	−	−	−	−	$0.23^{+0.15}_{-0.08}$	$48.2^{+4.6}_{-4.4}$	$1.5^{+0.4}_{-0.3}$
F21292-4953	PL	$21.0^{+0.6}_{-0.7}$	−	$-0.5^{+0.0}_{-0.0}$	−	−	−	−	−	$0.46^{+0.25}_{-0.13}$	$46.7^{+3.5}_{-3.6}$	$1.4^{+0.4}_{-0.3}$
F21295-4634	C2 1SAN	$1.1^{+0.7}_{-0.6}$	$0.3^{+0.2}_{-0.2}$	$-1.0^{+0.1}_{-0.1}$	−	$31.3^{+7.7}_{-6.1}$	$0.3^{+0.3}_{-0.2}$	−	$0.5^{+0.2}_{-0.1}$	$1.27^{+0.54}_{-0.44}$	$39.0^{+2.9}_{-2.2}$	$1.6^{+0.2}_{-0.3}$
F23389-6139	C2 1SA	$421.7^{+14.4}_{-14.6}$	$1.0^{+0.6}_{-0.7}$	$-1.4^{+0.0}_{-0.0}$	$0.4^{+0.0}_{-0.0}$	$91.9^{+6.8}_{-6.5}$	$0.7^{+0.6}_{-0.4}$	−	$3.0^{+0.2}_{-0.2}$	$0.86^{+0.26}_{-0.23}$	$44.7^{+2.7}_{-2.3}$	$1.3^{+0.3}_{-0.2}$

Figure 1. The observed data and preferred SED modelling of *IRAS* F23389-6139. The overlaid model exhibits two distinct FFA turnovers. Highlighted regions represent the 1σ uncertainty sampled by EMCEE.


Figure 2. A comparison of the 60 μm and 1.4 GHz luminosities of our 19 source sample and the Yun et al. (2001) sample. Luminosities have been estimated in the observed frame with no *k*-correction applied.

preferred model judged strictly by the Bayes evidence values. We include model specific features where possible as additional overlaid components. Highlighted regions of all plotted components represent the 1 (68 per cent) confidence interval.

To examine how our sample resided on the FRC, we compared it to the sample of 1809 objects of Yun et al. (2001). The Yun et al. (2001) sample cross-referenced the *IRAS* 2 Jy sample with the National Radio Astronomy (NRAO) Observatory Very Large Array (VLA) All-Sky Survey (Condon et al. 1998) to investigate the FRC over many orders of magnitude. To remain consistent with their work, no *k*-correction was applied. We see in Fig. 2 that our sample
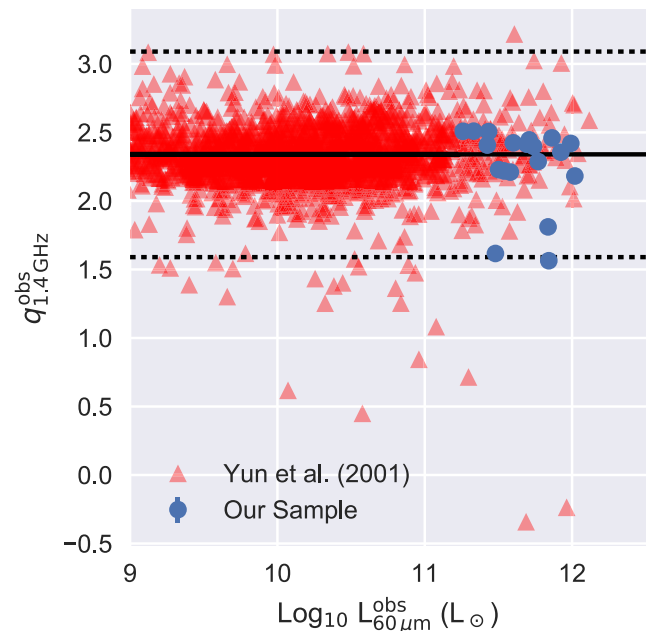
Figure 3. The FRC, as parametrized by the *q* parameter, of our sample and Yun et al. (2001). The solid horizontal line represents the mean *q* = 2.34, as calculated by Yun et al. (2001). The dotted lines represent the radio-excess (below) and IR-excess (above) objects, which we defined as three times the standard deviation (SD) of *q* (SD =0.25) from the Yun et al. (2001) sample.

is consistent with the trend seen by Yun et al. (2001), where only three of our objects (*IRAS* F06035-7102, *IRAS* F20117-3249 and *IRAS* F23389-6139) have a slightly elevated 1.4 GHz luminosity. The *q* parameter, which is the logarithmic ratio between the FIR flux and 1.4 GHz flux density of an object, is a further useful illustration of the FRC, where *q* is defined as

$$q \equiv \log_{10}\left(\frac{\text{FIR}}{3.75 \times 10^{12} \text{ W m}^{-2}}\right) -$$

$$\log_{10}\left(\frac{S_{1.4\text{ GHz}}}{\text{W m}^{-2}\text{ Hz}^{-1}}\right). \tag{11}$$

$S_{1.4\text{ GHz}}$ is the flux density at $\nu = 1.4$ GHz and FIR is defined as

$$\text{FIR} \equiv 1.26 \times 10^{-14}\left(2.58S_{60\ \mu\text{m}} + S_{100\ \mu\text{m}}\right)\text{ W m}^{-2}, \tag{12}$$

where $S_{60\ \mu\text{m}}$ and $S_{100\ \mu\text{m}}$ are the 60 and 100 μm band flux densities, respectively, from *IRAS* in Jy (Helou, Soifer & Rowan-Robinson 1985). The mean *q* value between 60 μm and 1.4 GHz is typically taken as 2.34 for star formation galaxies (Yun et al. 2001). Any deviation from this value can be a critical diagnostic of the physical processes driving some object. IR-excess sources (*q* > 3) may be highly obscured compact starburst galaxies or dust-enshrouded AGNs). Radio-excess objects (*q* < 1.6) are caused by excess radio emission originating from an AGN component in the galaxy (Yun et al. 2001). Some of the dispersion may be influenced in part by variation in extinction and dust temperature, as well as varying time-scales associated with different SFR indicators. We show in Fig. 3 the distribution of the *q* parameters as a function of 60 μm luminosity and highlight the regions that radio or infrared excess sources occupy.

Of our sample objects, *IRAS* F20117-3249 and *IRAS* F23389-6139 have *q* values (1.61 and 1.54, respectively) that are approaching the radio-excess region, indicating the potential presence of AGN activity in the observed 1.4 GHz radio continuum (see Fig. 3).

There is no classification of *IRAS* F20117-3249 available in the literature, although it has been designated as a galaxy by Paturel et al. (2003). *IRAS* F23389-6139, however, has been classified as a starburst based on optical imagery (Duc, Mirabel & Maza 1997) and infrared template modelling (Farrah et al. 2003). *IRAS* F06035-7102 also has a slightly elevated *q* parameter of 1.8. It has been classified in the literature as a starburst based on optical spectral features and infrared modelling (Saunders et al. 2000; Farrah et al. 2003).

5.2 Thermal fraction

The thermal fraction of a source is a measure of how much of the observed radio continuum is comprised of thermal free–free emission. At increasing frequencies, due to the steep spectral index of non-thermal synchrotron emission, the thermal free–free emission begins to dominate the total observed continuum. H II regions, which are traced by thermal free–free emission, are an excellent probe of current star formation. In the GHz regime, free–free emission represents roughly 5–10 per cent of the total radio continuum (Condon 1992; Murphy 2013) and due to its flat spectral index ($S_\nu \propto \nu^{-0.1}$), it is relatively difficult to isolate. The broad coverage of our radio-continuum SEDs however allows us to investigate this property. For each source, using the best-fitting model, we compute the total amount of thermal emission in order to derive appropriate nominal thermal fraction values.

We find at low frequencies the thermal fraction makes up only a small fraction of the total radio-continuum emission. This is similar to earlier studies (Condon & Yin 1990; Condon 1992; Price & Duric 1992), where at 1.4 GHz the typical thermal fraction was estimated to be around 10 per cent. In Fig. 4(a), we show that at 1.4 GHz the estimated thermal fraction is fairly constant at around 3–10 per cent, with the average thermal fraction being 3.8 per cent. This is in line with Murphy (2013), who find in a sample of 31 local starburst galaxies that the thermal fraction at 1.4 GHz is ≈5 per cent. At 40 GHz (Fig. 4b), the thermal fraction makes a much larger contribution to the modelled radio continuum, ranging between 35 and 80 per cent with an average of 38.8 per cent.

These thermal fractions, in principle, could be affected by missing interferometric flux at higher frequencies where free–free emission processes begin to become more dominate. However, we do not expect this to be an issue as our brightness temperature estimates (see Section 3.1.1) are above the lower limit for a face-on spiral galaxy and only approach this limit at the highest frequency in *Q* band.

5.3 Spectral curvature and emission measures

Similar to Clemens et al. (2010), the radio-continuum SEDs in our sample of objects are rarely characterized well by a simple power law. The broad frequency range covered by our data shows the presence of multiple bends or turnovers, which we attribute to the effects of FFA. Low-frequency data from the MWA GLEAM data show clear cases of low-frequency turnovers, as illustrated well by *IRAS* F01388-4618 and *IRAS* F23389-6139. At higher frequencies, we see in a subset of our sources evidence supporting a 'kink' in the radio-continuum spectrum. Likewise to the turnover at low frequency, we attribute this to a secondary FFA component with a higher optical depth.

Four objects from our sample had an evidence value that most supported a 'simple' model (a power law or the simple normalization of synchrotron and free–free power-law components). Of these four, objects only *IRAS* F01419-6826 had a competing higher order
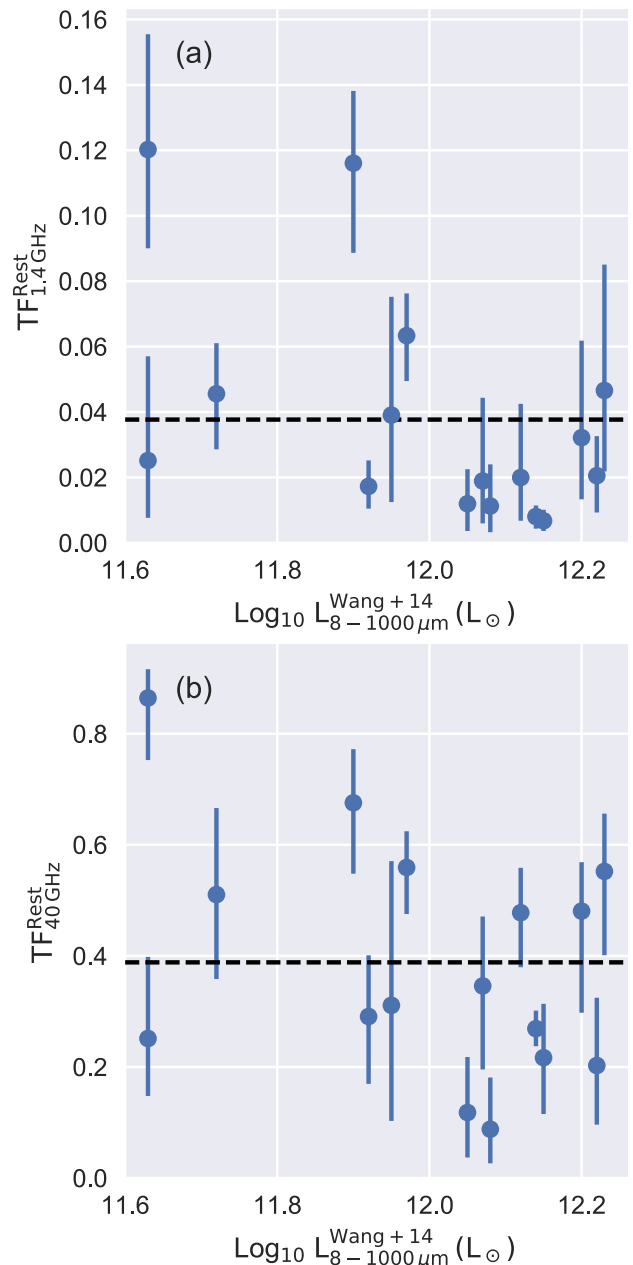
Figure 4. A comparison between the total infrared emission and the estimated thermal fraction of the rest frame at 1.4 GHz (a) and at 40 GHz (b). Dashed horizontal lines represent the average thermal fraction.

model. The remaining 15 objects all had higher order (i.e. turnover due to FFA) models most supported by the evidence, where only source *IRAS* F03068-5346 had a 'simple' competing model.

A common feature seen in our SEDs is the steepening of the radio-continuum spectrum between the 4 and 10 GHz regime. A similar effect was also seen by Clemens et al. (2008, 2010) and Leroy et al. (2011). In cases where the MWA GLEAM low-frequency measurements indicate a low-frequency turnover, this steepening is often modelled by an additional component of FFA-attenuated synchrotron and free–free emission. This higher order complexity is supported by both an improved χ^2 statistic and $\mathcal{Z}$ value.

The turnover frequency due to FFA is dependent on where the optical depth reaches unity. Generally, it is assumed that the emitting

Table 6. An overview of the emission measures (EM) derived for each source from the model most supported by the evidence. Objects without an emission measure constrained are marked by '–'.

Source *IRAS*	EM_1 10^6 cm^{-6} pc	EM_2 10^6 cm^{-6} pc
F00198-7926	0.016	13.851
F00199-7426	–	0.067
F01388-4618	0.021	–
F02364-4751	0.017	–
F03068-5346	0.003	–
F04063-3236	0.029	15.762
F06021-4509	0.038	6.88
F06035-7102	–	0.044
F06206-6315	0.059	7.1
F18582-5558	–	10.599
F20117-3249	–	0.858
F20445-6218	0.01	–
F21178-6349	0.043	–
F21295-4634	–	0.08
F23389-6139	0.044	3.11

H II regions form a cylinder orientated along of line of sight with constant temperature and density (Condon 1992). In such scenarios, the free–free opacity is well approximated by

$$\tau_\nu = 3.28 \times 10^{-7} \left(\frac{T_e}{10^4\,K} \right) \left(\frac{\nu}{GHz} \right)^{-2.1} \left(\frac{EM}{pc\,cm^{-6}} \right), \quad (13)$$

where T_e is the electron temperature of the H II emitting region, typically taken as 10^4 K, and EM is the emission measure, defined as

$$\frac{EM}{pc\,cm^{-6}} = \int_{los} \left(\frac{N_e}{cm^{-3}} \right)^2 d \left(\frac{s}{pc} \right). \quad (14)$$

EM is the integral of the electron density along the line of sight of a H II region of depth s. Using the above form, for frequencies above the turnover frequency ν_t, the free–free spectrum follows a power law of $\alpha \sim -0.1$. Once the optical depth reaches unity, the spectrum transitions to the Rayleigh–Jeans law, described well by ν^2. Using the turnovers constrained by our modelling, we have estimated the EMs of our sources, outlined in Table 6, using equation (14). We label the corresponding EM of $\nu_{t,1}$ and $\nu_{t,2}$ for all models as EM_1 and EM_2, respectively.

For systems with multiple intense starburst regions that have been integrated over by a large synthesized radio-telescope beam, their superposition of radio-continuum features will form the observed SED. The orientation of such regions will play a crucial role in the spectral curvature across a broad frequency range. Regions that are small and deep will possess much higher EMs than those which are more widespread and shallow relative to our observing angle. Although the EM is tied to the spatial size of an object, which can vary as a function of frequency with increasing amounts of diffuse synchrotron, we have no evidence to suggest we are resolving our sample, particularly at high frequency where we have obtained critical short spacing data.

5.4 FIR -to-radio correlation

The radio-continuum emission is considered an ideal tracer of star formation, as it is not effected by dust attenuation. In terms of the local Universe ($z < 0.2$), it is fairly well calibrated by bootstrapping the radio-continuum SFR against the FIR SFR via the FRC.

Although understood well in the local Universe, it is unknown whether the FRC will evolve with increasing redshift. As outlined by Murphy (2009), due to the changing composition of the radio continuum with increasing frequency (which is what would be Doppler shifted to lower frequency) and synchrotron suppression effects that scale with $(1 + z)^4$ caused by IC losses, it is thought that the FRC will need to be 'recalibrated' to be compatible with the high redshift Universe. Mao et al. (2011), however, see no evidence of evolution in the FRC up to $z \sim 2$ using image stacking techniques, suggesting that the FRC is more physically complex than first thought. As we show in Fig. 2, our sample of objects follows the FRC.

The synchrotron and free–free emission mechanisms that make up the radio continuum are both tracers of star formation across different time-scales. Given the posterior distribution sampled by EMCEE of the most supported model of each source, we compare in Fig. 5 the total FIR (taken from Wang et al. 2014) against the decomposed synchrotron and free–free components at 1.4 and 40 GHz. For each comparison, we also include the results of a non-weighted linear fit against multiple realizations (N=1000) of our data, drawn randomly from the posterior distribution. Highlighted regions represent the 1σ uncertainty of the best-fitting parameters of this process.

The total FIR correlates well with the modelled synchrotron luminosity for all sources at 1.4 GHz, as demonstrated in Fig. 5(a). This can simply be attributed to synchrotron emission dominating the radio continuum at 1.4 GHz (Condon 1992; Yun et al. 2001; Bell 2003; Murphy et al. 2006). The two outlying objects, whose synchrotron luminosities are in excess of 10^{24} W Hz^{-1}, are *IRAS* F20117-3249 and *IRAS* F23389-6139.

Free–freeemission is a more reliable probe of SFR with these increasing redshifts as it directly tracers H II regions ionized by nearby HMSs and is unaffected by IC losses. Identifying the free–free emission at low frequencies, where it contributes $\sim$5–10 per cent at 1.4 GHz, is difficult and few studies have successfully isolated its signature (Price & Duric 1992; Clemens et al. 2010; Murphy et al. 2010, 2012; Galvin et al. 2016). This is demonstrated in the top panel of Fig. 5(b), where there is considerable uncertainty associated with the constrained free–free luminosity at 1.4 GHz.

With increasing frequencies, there is a change in the composition of the radio continuum. Synchrotron emission, due to its steep spectral index, quickly begins to weaken. We show in Figs 5(c)–(e) that though there is still a strong correlation between the total infrared and the estimated synchrotron luminosity, it is one with increased uncertainty when compared to the equivalent relation constrained at 1.4 GHz (Fig. 5a). The correlation between the total infrared and free–free luminosity at 40 GHz (Fig. 5f) is far more constrained than it was at 1.4 and 5.0 GHz (Figs 5 b–d).

In Table 7, we list the best-fitting values from a simple linear regression between the total infrared (in units of L$_\odot$) and the decomposed synchrotron and free–free luminosity components at 1.4, 5.0 and 40 GHz (in units of W Hz^{-1}). Errors were estimated by drawing 1000 realizations of the luminosities from the posterior distribution sampled by EMCEE. We find these results acceptable, given that we have less than one order of magnitude of range in the total infrared luminosities.

Price & Duric (1992) performed a similar analysis for a sample of 31 galaxies. Their study used a single model equivalent to equation (2) and found that the decomposed synchrotron and free–free components are tightly correlated to the FIR across roughly three orders of magnitude. At 5.0 GHz, they estimate the gradient of the synchrotron-FIR and free–free-FIR correlations to be 1.33 ± 0.1 and 0.93 ± 0.02, respectively. These are comparable to the correlations derived above, particularly the synchrotron–TIR component
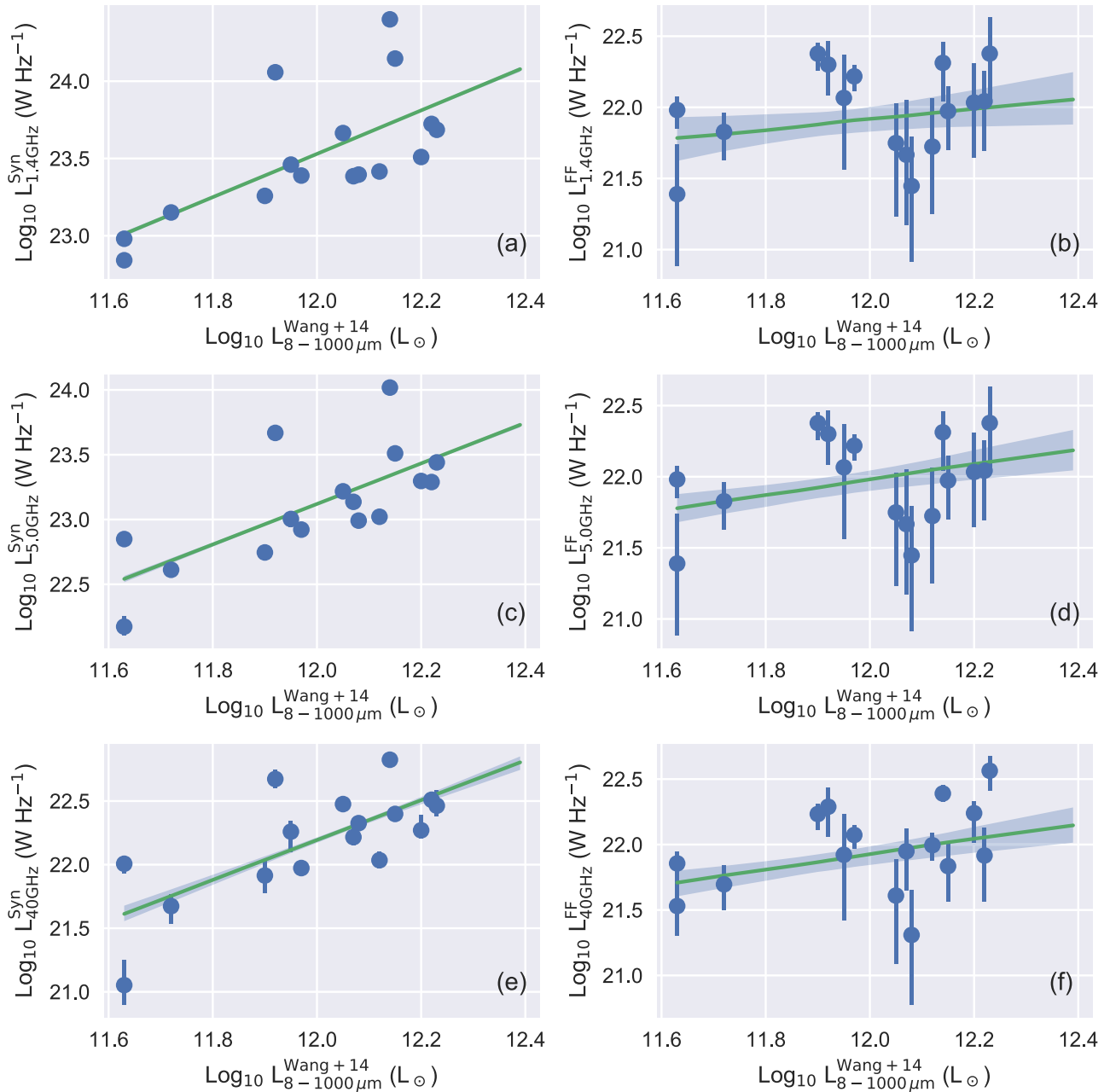
Figure 5. A comparison between the total infrared derived luminosity, as presented by Wang et al. (2014), and the constrained synchrotron *(a,c,e)* and free–free luminosities *(b,d,f)* at 1.4, 5.0 and 40 GHz of sources in our sample. The green line and its highlighted region represent a non-weighted linear regression and the corresponding 1σ uncertainty region determined from 1000 realizations.

at $\nu = 5.0\,\mathrm{GHz}$. Although we are using the total infrared luminosities, defined as the bolometric luminosity from 8 to 1000 μm, derived by Wang et al. (2014) and their IR template fitting routines, the bulk of emission for SFGs in this regime is emitted in the FIR (Helou et al. 1988; Condon 1992). This difference would influence the normalization component that are not being compared here.

We acknowledge that these correlations may be partly a result of our sample selection criteria. By ensuring that sources were selected such that there was no radio or infrared excess objects, as measured by deviation of their q parameter, there may be a selection bias. If sources were purposely selected to be on the FRC, then the components of the radio-continuum modelling are also likely to

follow similar trends. However, the initial constraints on q were broad enough to be considerably larger than the intrinsic scatter in the original correlation (see Fig. 3) and those reported here.

6 DISCUSSION

6.1 Spectral curvature – physical origin?

Sixteen objects in our sample show spectral characteristics that are not consistent with a simple power-law model. An inconsistent flux calibration scale may also influence spectral features when comparing data across a broad frequency range. For ATCA data,

Table 7. The fitted gradient and normalization components of a non-weighted linear fit between the total infrared and decomposed radio-continuum luminosities. Synchrotron and free–free luminosity components are labelled as 'Syn' and 'FF', respectively. We also provide the mean and standard deviation of the q parameter, derived using the total infrared luminosity from Wang et al. (2014), for each of the correlations.

ν (GHz)	Emission	Gradient	Norm. ($\mathrm{Log_{10}\,W\,Hz^{-1}}$)	$q \pm \sigma_q$
1.4	Syn	$1.40^{+0.03}_{-0.04}$	$6.68^{+0.47}_{-0.41}$	2.53 ± 0.38
5.0	Syn	$1.56^{+0.06}_{-0.05}$	$4.36^{+0.62}_{-0.66}$	2.94 ± 0.40
40.0	Syn	$1.57^{+0.13}_{-0.15}$	$3.39^{+1.77}_{-1.56}$	3.87 ± 0.39
1.4	FF	$0.33^{+0.43}_{-0.33}$	$17.95^{+3.92}_{-5.10}$	4.09 ± 0.33
5.0	FF	$0.53^{+0.27}_{-0.25}$	$15.60^{+2.93}_{-3.27}$	4.04 ± 0.34
40.0	FF	$0.58^{+0.25}_{-0.23}$	$14.97^{+2.74}_{-2.97}$	4.09 ± 0.34

PKS 1934-638 is almost exclusively used as a flux calibrator. This gigahertz peaked spectrum source has been well characterized from low to high frequency, and is estimated to be absolute spectrum of 3C286 and 3C295 on the Baars et al. (1977) scale (Reynolds 1994; Partridge et al. 2016). As it was used to provide a flux calibration scale for all ATCA data from 2.1 to 25 GHz for sources in our sample, it is unlikely that high-frequency kinks between 4 and 10 GHz are due to mis-matched flux scale.

At the time of observing the high-frequency Q band data, Uranus was the preferred flux calibrating source at ATCA. The flux density accuracy at these frequencies is estimated to be within 10 per cent. An overestimated flux density at these frequencies would have the effect of increasing the amount of free–free emission while model fitting, producing a more pronounced flattening at higher frequencies. Therefore, we have added an additional 10 per cent error in quadrature as a measure to counteract this effect. Low-frequency data from SUMSS and MWA GLEAM DR1 both use the Molonglo reference catalogue (MRC; Large et al. 1981; Large, Cram & Burgess 1991) in large part to craft a flux calibration scale that is accurate to 2–3 per cent on the Baars et al. (1977) scale. To account for any residual flux calibration mismatch, we inject an additional 5 per cent error in quadrature for all flux density measurements obtained through NED, including measurements from SUMSS, or archived ATCA observations (Table 3).

Therefore, the curvature features we see in our modelling, we believe, are physical in origin. When the derived emission measures (Table 6) are compared to similar studies we find that they are consistent. Clemens et al. (2010) studied a sample of 20 luminous and ultra LIRGs using data from 244 MHz to frequencies in excess of 23 GHz. Although their SEDs are more sparsely sampled than those in this study, they find evidence that suggests multiple FFA components with varying optical depths. They find emission measures in the range of $(0.12–140) \times 10^6\ \mathrm{cm^{-6}\ pc}$. Similarly, observations using MERLIN of compact sources in M82 at 408 MHz presented by Wills et al. (1997) are in agreement with emission measures derived from low-frequency turnovers for our sample. At higher frequencies, Neff & Ulvestad (2000) also find emission measures in excess of $10^8\ \mathrm{cm^{-6}\ pc}$ for compact H II regions and supernova remnants observed in the NGC 4038 and NGC 4039 merger system.

Arp 220, the closest ultra-LIRG, has observational evidence of a double starburst nucleus thought to be powered by a recent merger (Downes & Solomon 1998; Smith et al. 1998; Engel et al. 2011). Using radio recombination lines to constrain turnover features, Anantharamaiah et al. (2000) argue that the radio-continuum SED of Arp 220 is best characterized by three regions of star formation with turnover frequencies at roughly 0.5, 1.4 and 40 GHz. Using their resolved data allowed them to place further constraints on the emitting size and density of the three emission measures, which they modelled as 1.3×10^5, 5.0×10^6 and $6.3 \times 10^9\ \mathrm{cm^{-6}\ pc}$. Recently, Kapinska et al. (2017) performed radio-continuum modelling of NGC 253 from 76 MHz to 11 GHz. They found that the galaxy was best described as the sum of a discrete central starburst region, modelled as an internally free–free absorbed synchrotron plasma, with an additional synchrotron component that flattens at low frequency.

The effects of FFA on the radio continuum have been investigated by Lenc & Tingay (2009) and Rampadarath et al. (2014) on resolved sources embedded within the nearby starburst galaxies NGC 4945 and NGC 253. Both studies find evidence of FFA and a range of turnover frequencies between 2 and 10 GHz. Lenc & Tingay (2009) also note that the free–free opacity is highest towards the nucleus of NGC 4945, but varies significantly. This implies a clumpy composition of star-forming regions throughout the system.

More broadly, resolved multiwavelength studies of intense starburst galaxies, in the same class as those in our sample, also show multiple, distinct clumps. Farrah et al. (2001) used the Wide Field Planetary Camera 2 (WFPC2) on the *Hubble Space Telescope (HST)* to study 23 Ultra-LIRGs (ULIRGs). They find that most observed sources are in some stage of merger with stellar population synthesis modelling, suggesting ages less than several Gyr. Colour maps (based on multiple filters) show a number of distinct 'knots' that are clearly distinguished from the surrounding environment that are likely regions of intense starburst activity. Similar *HST I*-band imaging by Borne et al. (2000) also shows that U/LIRGs are often interacting systems in some stage of merger.

6.2 Effects of FFA on low-frequency extrapolations

Euclidean normalized radio source counts of extragalactic objects are a useful cosmological tool (de Zotti et al. 2010). Previous to low-frequency SKA pathfinder projects and their all-sky surveys, including MWA and LOFAR, the radio sky at low frequency was extrapolated from slightly higher frequency surveys and assumed power laws. Although useful as an initial estimate, this approach ignores low-frequency turnovers caused by free–free absorption. Understanding the behaviour of starburst galaxies, and any deviations from the extrapolated optically thin spectrum, will be important for interpreting the well-known uptick in the Euclidean normalized radio source counts (Gruppioni et al. 2003; Seymour et al. 2008).

In our sample, we find that most objects have a well-characterized turnover component. In Fig. 6, we compare the effects of omitting this feature and the effects that it may have on simple extrapolation. Flux densities without FFA were obtained by removing the frequency-dependent τ parameter from the most preferred model. We show an example of this in Fig. 7.

At 200 MHz (Fig. 6), there is only a small difference to the estimated radio continuum when ignoring the effects of FFA. All but one of our 17 sources with a low-frequency turnover are below a suppression factor of 5, with the average being ∼2.2 (ie. without FFA, the radio continuum would be 2.2 times higher than what is observed). At 80 MHz, we find that FFA has a far more significant effect on the observed fluxes. Using the applied modelling, we find that at 80 MHz (Fig. 6) the estimated radio continuum without FFA is, on average, ∼12 times larger than the observed SED.

Including curvature due to FFA for SFG-type sources when estimating low-frequency source counts and confusion limits will be
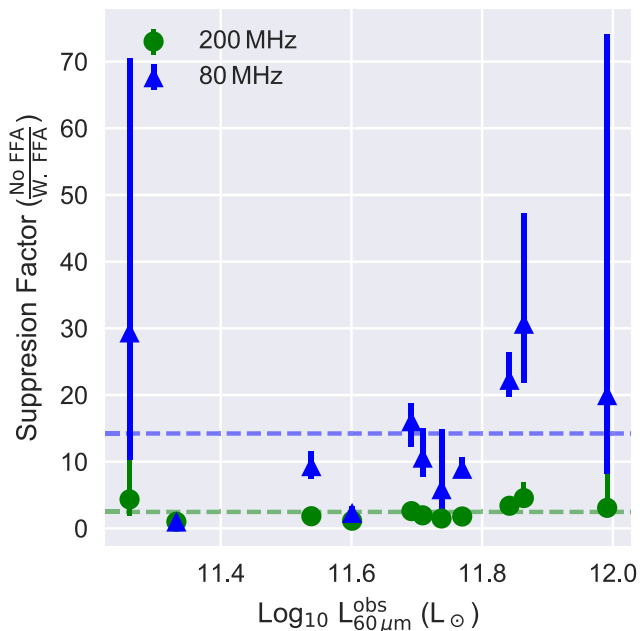
Figure 6. A comparison between the observed 60 μm luminosities and the ratio of the observed radio continuum with and without the effects of FFA at 80 and 200 MHz. The dashed horizontal lines show the average suppression factor for each group.
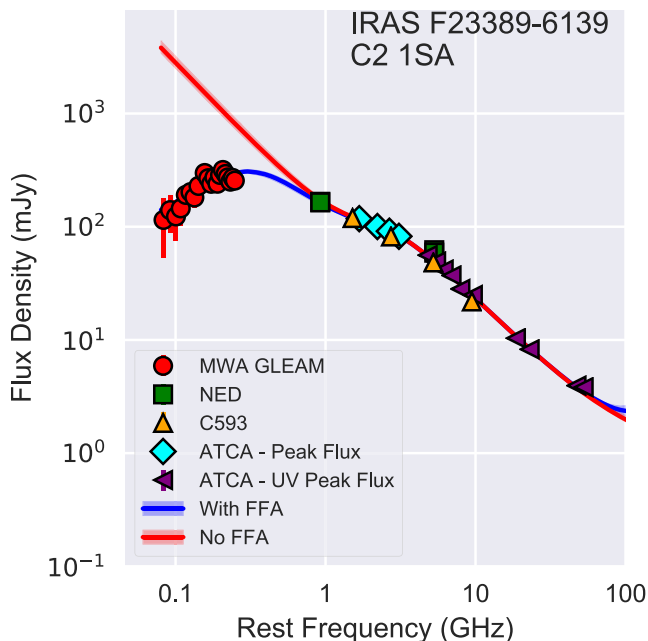
Figure 7. The constrained SED of *IRAS* F23389-6139 with the effects of FFA at low frequencies removed. All other constrained parameters are unchanged.

important. Earlier studies have typically used simple power-law models with varying spectral indices when extrapolating fluxes between frequencies (Waldram et al. 2007; Franzen et al. 2016). Similarly, Wilman et al. (2008) performed a semi-empirical simulation of the radio continuum sky out to $z = 20$. In their simulation, a turnover due to FFA was assumed at 1 GHz for all starburst galaxies. Our sample, which is constructed to be representative of high redshift starburst galaxies, has turnovers between 90 and 500 MHz

(if they were detected). Incorporating our turnover frequencies into the assumed model of Wilman et al. (2008) will have the effect of *increasing* the modelled flux densities at low frequencies. Ga lvin et al. (in preparation) are exploring the degree of change and how confusion limits could be effected.

6.3 Synchrotron spectral index

The mean modelled synchrotron spectral index in our sample is $\alpha = -1.06$, noticeably steeper than the canonical spectral index of $\alpha \sim -0.8$ often assumed for SFGs (Condon 1992). This is based on the well-constrained power-law slope of the distribution of cosmic rays we observe at Earth that directly relates to the synchrotron spectral index. This difference is larger than our modelling uncertainties and seems a real outcome of modelling. We consider here four mechanisms that could explain the steeper than Milky Way spectral index: (i) electron cooling via IC losses, (ii) ageing of relativistic electron energy distribution, (iii) a steeper power law in the relativistic electron energy distribution or (iv) a different galaxy morphology for extreme starbursts affecting cosmic ray diffusion. We consider (i) to be unlikely as IC losses are weak at low redshift and competing against other losses (Lacki & Thompson 2010). Ageing of the starburst is unlikely, as the IR luminosities (which is a more instantaneous tracer of SFR) are still high.

There is some evidence in the literature from GeV and TeV observations of galaxies with higher SFR having a steeper cosmic ray power-law index (e.g. Wang & Fields 2016). This steeper cosmic ray power-law index would then infer a steeper synchrotron spectrum. Our SFGs have even higher SFRs so might be expected to have synchrotron spectral indices as steep as we see here. Interestingly, in the case where a single power law is preferred over multiple components with turnovers the fitted spectral index is lower and closer to the canonical value. One explanation for this, and the lower spectral indices typically seen in deep surveys (Ibar et al. 2009; Huynh et al. 2012), is that simple two- to three-point broad-band spectral indices miss the complexity of spectral structure we observe here and 'average' over a steeper power law with multiple turnover components.

The final possibility is that powerful stardusts are fundamentally different to lower SFR galaxies previously studied in detail. Lacki & Thompson (2010) describe scenarios where 'puffy' starburst galaxies, whose volume density is far less than compact starbursts, can exhibit a steeper cosmic ray distribution index by having a far higher scaleheight for the cosmic ray distribution. Therefore, we suggest that the steep synchrotron spectral indices modelled in our sample of sources are caused by either a steeper cosmic ray distribution index or a physical difference in the nature of these galaxies compared to nearby lower SFR SFGs.

7 CONCLUSION

We have modelled the radio continuum across a broad frequency range (70 MHz–48 GHz) for a sample of 19 LIRGs, selected specifically to represent the types of objects to be discovered by SKA and its pathfinder projects at high redshifts. We find that:

(i) in our sample of 19 objects, the radio continuum of only three (16 per cent) sources was characterized well by a single power-law component over a broad frequency range;

(ii) 11 objects show evidence of a low-frequency turnover ($\nu < 800$ MHz), with 10 exhibiting features between 400 MHz and 6.5 GHz that are consistent with a higher frequency turnover. Six

sources in our sample of 19 show evidence of both a low- and mid- to high-frequency turnover. These could be explained by considering free–free absorption processes acting across multiple regions of star formation, each with different optical depths, that are then integrated over by the large radio synthesized beam;

(iii) the intrinsic components that make up the radio continuum are correlated with the FIR, with the Syn-IR correlations being steeper than the FF-IR trends, similar to the FRC used to calibrate current 1.4 GHz SFR tracers; and

(iv) without accounting for the effects of FFA the low-frequency radio emission of faint starburst galaxies is susceptible to being over estimated by as much as a factor of 30 when using a simple power-law scaling from a higher frequency, which may influence estimations of low-frequency source counts;

(v) the mean synchrotron spectral index of our sample is $\alpha = -1.06$, which is steeper than the canonical value of $\alpha = -0.8$. We suggest that this is associated with a steeper cosmic ray distribution index.

In part 2 of this series of papers, we will present the optical integral field spectroscopy obtained for our sample of 19 LIRGs, focusing on the resolved distribution of the Balmer stellar emission lines that trace the same emitting matter as free–free emission, and dust-corrected Hα SFRs.

ACKNOWLEDGEMENTS

REFERENCES

Ambikasaran S., Foreman-Mackey D., Greengard L., Hogg D. W., O'Neil M., 2015, ITPAM, 38, 252
Anantharamaiah K. R., Viallefond F., Mohan N. R., Goss W. M., Zhao J. H., 2000, ApJ, 537, 613
Baars J. W. M., Genzel R., Pauliny-Toth I. I. K., Witzel A., 1977, A&A, 61, 99
Bell E. F., 2003, ApJ, 586, 794
Borne K. D., Bushouse H., Lucas R. A., Colina L., 2000, ApJ, 529, L77
Callingham J. R. et al., 2015, ApJ, 809, 168
Clemens M. S., Vega O., Bressan A., Granato G. L., Silva L., Panuzzo P., 2008, A&A, 477, 95
Clemens M. S., Scaife A., Vega O., Bressan A., 2010, MNRAS, 405, 887
Condon J. J., 1992, ARA&A, 30, 575
Condon J. J., Yin Q. F., 1990, ApJ, 357, 97
Condon J. J., Cotton W. D., Greisen E. W., Yin Q. F., Perley R. A., Taylor G. B., Broderick J. J., 1998, AJ, 115, 1693
de Zotti G., Massardi M., Negrello M., Wall J., 2010, A&AR, 18, 1
Dopita M., Hart J., McGregor P., Oates P., Bloxham G., Jones D., 2007, Ap&SS, 310, 255
Dopita M. et al., 2010, Ap&SS, 327, 245
Downes D., Solomon P. M., 1998, ApJ, 507, 615
Duc P.-A., Mirabel I. F., Maza J., 1997, A&AS, 124
Engel H., Davies R. I., Genzel R., Tacconi L. J., Sturm E., Downes D., 2011, ApJ, 729, 58
Farrah D. et al., 2001, MNRAS, 326, 1333
Farrah D., Afonso J., Efstathiou A., Rowan-Robinson M., Fox M., Clements D., 2003, MNRAS, 343, 585
Feroz F., Hobson M. P., Bridges M., 2009, MNRAS, 398, 1601
Foreman-Mackey D., Hogg D. W., Lang D., Goodman J., 2013, PASP, 125, 306
Franzen T. M. O. et al., 2016, MNRAS, 459, 3314
Frater R. H., Brooks J. W., Whiteoak J. B., 1992, J Electrical Electron Eng. Aust., 12, 103
Galvin T. J., Seymour N., Filipović M. D., Tothill N. F. H., Marvil J., Drouart G., Symeonidis M., Huynh M. T., 2016, MNRAS, 461, 825
Gooch R., 1996, in Jacoby G. H., Barnes J., eds, ASP Conf. Ser., Vol. 101, Astronomical Data Analysis Software and Systems V. Astron. Soc. Pac., San Francisco, p. 80
Goodman J., Weare J., 2010, Commun Appl Math Comput Sci, 5, 65
Gregory P. C., Vavasour J. D., Scott W. K., Condon J. J., 1994, ApJS, 90, 173
Gruppioni C., Pozzi F., Zamorani G., Ciliegi P., Lari C., Calabrese E., La Franca F., Matute I., 2003, MNRAS, 341, L1
Hancock P. J., Murphy T., Gaensler B. M., Hopkins A., Curran J. R., 2012, MNRAS, 422, 1812
Helou G., Soifer B. T., Rowan-Robinson M., 1985, ApJ, 298, L7
Helou G., Khan I. R., Malek L., Boehmer L., 1988, ApJS, 68, 151
Hildebrand R. H., 1983, QJRAS, 24, 267
Hughes A., Wong T., Ekers R., Staveley-Smith L., Filipovic M., Maddison S., Fukui Y., Mizuno N., 2006, MNRAS, 370, 363
Hughes A., Staveley-Smith L., Kim S., Wolleben M., Filipović M., 2007, MNRAS, 382, 543
Hurley-Walker N. et al., 2017, MNRAS, 464, 1146
Huynh M. T., Hopkins A. M., Lenc E., Mao M. Y., Middelberg E., Norris R. P., Randall K. E., 2012, MNRAS, 426, 2342
Ibar E., Ivison R. J., Biggs A. D., Lal D. V., Best P. N., Green D. A., 2009, MNRAS, 397, 281
Ivison R. J. et al., 2010, A&A, 518, L31
Jarvis M. et al., 2015, Proc. Sci., The Star-Formation History of the Universe with the SKA. SISSA, Trieste, PoS(AASKA14)068
Kapińska A. D. et al., 2017, ApJ, 838, 68
Kass R. E., Raftery A. E., 1995, J. Am. Stat. Assoc., 90, 773
Klaas U. et al., 2001, A&A, 379, 823
Komatsu E. et al., 2009, ApJS, 180, 330
Lacki B. C., Thompson T. A., 2010, ApJ, 717, 196
Large M. I., Mills B. Y., Little A. G., Crawford D. F., Sutton J. M., 1981, MNRAS, 194, 693
Large M. I., Cram L. E., Burgess A. M., 1991, Observatory, 111, 72
Lenc E., Tingay S. J., 2009, AJ, 137, 537
Leroy A. K. et al., 2011, ApJ, 739, L25
Lonsdale C. J. et al., 2009, IEEE Proc., 97, 1497
Mao M. Y., Huynh M. T., Norris R. P., Dickinson M., Frayer D., Helou G., Monkiewicz J. A., 2011, ApJ, 731, 79
Mauch T., Murphy T., Buttery H. J., Curran J., Hunstead R. W., Piestrzynski B., Robertson J. G., Sadler E. M., 2003, MNRAS, 342, 1117
Mauch T. Murphy T., Buttery H. J., Curran J., Hunstead R. W., Piestrzynski B., Robertson J. G., Sadler E. M., 2013, VizieR Online Data Catalog, 8081, 0
Middelberg E., Sault R. J., Kesteven M. J., 2006, PASA, 23, 147

Mooley K. P. et al., 2016, ApJ, 818, 105

Moshir M., 1990, in IRAS Faint Source Catalogue, version 2.0 (1990), p. 0

Murakami H. et al., 2007, PASJ, 59, S369

Murphy E. J., 2009, ApJ, 706, 482

Murphy E. J., 2013, ApJ, 777, 58

Murphy E. J. et al., 2006, ApJ, 651, L111

Murphy E. J. et al., 2010, ApJ, 709, L108

Murphy E. J. et al., 2012, ApJ, 761, 97

Neff S. G., Ulvestad J. S., 2000, AJ, 120, 670

Niklas S., Klein U., Wielebinski R., 1997, A&A, 322, 19

Norris R. P. et al., 2011, PASA, 28, 215

Partridge B., López-Caniego M., Perley R. A., Stevens J., Butler B. J., Rocha G., Walter B., Zacchei A., 2016, ApJ, 821, 61

Paturel G., Petit C., Prugniel P., Theureau G., Rousseau J., Brouty M., Dubois P., Cambrésy L., 2003, A&A, 412, 45

Prandoni I., Seymour N., 2015, Proc. Sci., Revealing the Physics and Evolution of Galaxies and Galaxy Clusters with SKA Continuum Surveys. SISSA, Trieste, PoS(AASKA14)067

Price R., Duric N., 1992, ApJ, 401, 81

Rampadarath H., Morgan J. S., Lenc E., Tingay S. J., 2014, AJ, 147, 5

Rasmussen C. E., Williams C. K. I., 2006, Gaussian Processes for Machine Learning. MIT Press, Cambridge, MA, p. 248

Reynolds J., 1994, A revised flux scale for the AT compact array. Tech. Rep. AT/39.3/040, ATNF Memo

Sault R. J., Wieringa M. H., 1994, A&AS, 108, 585

Sault R. J., Teuben P. J., Wright M. C. H., 1995, in Shaw R. A., Payne H. E., Hayes J. J. E., eds, ASP Conf. Ser., Vol. 77, Astronomical Data Analysis Software and Systems IV. Astron. Soc. Pac., San Francisco, p. 433

Saunders W. et al., 2000, MNRAS, 317, 55

Seymour N. et al., 2008, MNRAS, 386, 1695

Smith H. E., Lonsdale C. J., Lonsdale C. J., Diamond P. J., 1998, ApJ, 493, L17

Smith D. J. B. et al., 2013, MNRAS, 436, 2435

Tingay S. J. et al., 2013, PASA, 30, e007

Waldram E. M., Bolton R. C., Pooley G. G., Riley J. M., 2007, MNRAS, 379, 1442

Wang X., Fields B. D., 2016, ApJ, preprint (arXiv:1612.07290)

Wang L., Rowan-Robinson M., Norberg P., Heinis S., Han J., 2014, MNRAS, 442, 2739

Wayth R. B. et al., 2015, PASA, 32, e025

Wills K. A., Pedlar A., Muxlow T. W. B., Wilkinson P. N., 1997, MNRAS, 291, 517

Wilman R. J. et al., 2008, MNRAS, 388, 1335

Wilson W. E. et al., 2011, MNRAS, 416, 832

Yamamura I., Makiuti S., Ikeda N., Fukuda Y., Oyabu S., Koga T., White G. J., 2010, VizieR Online Data Catalog, 2298

Yun M. S., Reddy N. A., Condon J. J., 2001, ApJ, 554, 803

APPENDIX A: FLUX DENSITY MEASUREMENTS

In this section, we list the flux density measurements used throughout the modelling described in Sections 2 and 3. For measurements acquired through the NED data base, we include references to the source of the measurements (see Tables A1–A3).

Table A1. An overview of all radio-continuum measurements obtained from the MWA GLEAM catalogue (Hurley-Walker et al. 2017). Otherwise, sources with only four measurements at frequencies of 88, 119, 155 and 200 MHz were obtained using the PRIORISED option available in the AEGEAN packages. Sources with upwards of 20 measurements were taken directly from the MWA GLEAM project (Wayth et al. 2015).

Source IRAS	76 MHz (mJy)	84 MHz (mJy)	88 MHz (mJy)	92 MHz (mJy)	99 MHz (mJy)	107 MHz (mJy)	115 MHz (mJy)	119 MHz (mJy)	122 MHz (mJy)	130 MHz (mJy)	143 MHz (mJy)	151 MHz (mJy)
F00198-7926	47.9 ± 121.6	–	–	237.4 ± 97.8	226.4 ± 106.4	101.2 ± 63.3	5.7 ± 48.1	–	179.9 ± 50.0	218.9 ± 47.0	39.5 ± 34.0	156.4 ± 39.6
F00199-7426	–	–	141.0 ± 53.9	–	–	–	–	25.6 ± 25.6	–	–	–	–
F01268-5436	361.9 ± 81.2	237.9 ± 60.0	–	83.7 ± 48.9	28.0 ± 48.6	87.7 ± 38.3	122.5 ± 33.4	–	123.9 ± 30.2	135.5 ± 29.4	147.5 ± 30.0	112.1 ± 25.7
F01388-4618	–	–	32.4 ± 32.4	–	–	–	–	15.2 ± 15.2	–	–	–	–
F01419-6826	–	–	31.0 ± 31.0	–	–	–	–	36.6 ± 14.5	–	–	–	–
F02364-4751	32.5 ± 73.8	139.6 ± 54.3	–	73.6 ± 45.5	27.3 ± 43.3	2.3 ± 35.7	68.0 ± 29.6	–	98.8 ± 27.7	69.2 ± 24.7	52.4 ± 17.5	41.4 ± 15.4
F03068-5346	–	170.0 ± 52.5	–	46.3 ± 45.3	77.9 ± 44.0	98.3 ± 33.3	91.4 ± 28.3	–	74.1 ± 25.2	83.2 ± 24.3	80.2 ± 21.5	38.9 ± 18.7
F03481-4012	195.1 ± 76.5	80.4 ± 59.0	–	93.2 ± 52.3	114.5 ± 48.6	138.7 ± 37.3	69.4 ± 29.9	–	75.0 ± 28.2	64.0 ± 25.0	76.0 ± 24.8	66.4 ± 22.2
F04063-3236	–	–	–	–	–	54.2 ± 37.3	34.9 ± 30.1	–	29.4 ± 28.1	20.7 ± 25.6	18.3 ± 21.3	44.4 ± 19.0
F06021-4509	–	–	38.7 ± 38.7	–	–	–	–	20.9 ± 20.9	–	–	–	–
F06035-7102	898.0 ± 144.6	568.7 ± 97.2	–	686.1 ± 101.7	712.2 ± 106.6	634.5 ± 81.8	530.8 ± 67.7	–	536.6 ± 65.2	510.9 ± 62.0	474.8 ± 56.0	465.7 ± 54.3
F06206-6315	–	–	30.8 ± 30.8	–	–	–	–	14.3 ± 14.3	–	–	–	–
F18582-5558	–	–	40.4 ± 40.4	–	–	–	–	21.8 ± 21.8	–	–	–	–
F20117-3249	–	–	201.0 ± 47.8	–	–	–	–	131.0 ± 39.2	–	–	–	–
F20445-6218	–	–	43.7 ± 43.7	–	–	–	–	20.0 ± 20.0	–	–	–	–
F21178-6349	–	–	47.9 ± 47.9	–	–	–	–	20.6 ± 20.6	–	–	–	–
F21292-4953	40.8 ± 80.3	140.7 ± 65.0	–	50.5 ± 56.8	51.1 ± 47.1	135.1 ± 39.2	61.0 ± 29.8	–	96.4 ± 26.8	79.9 ± 25.4	71.2 ± 19.3	51.1 ± 16.5
F21295-4634	–	–	28.7 ± 28.7	–	–	–	–	17.4 ± 17.4	–	–	–	–
F23389-6139	114.8 ± 62.1	140.2 ± 50.7	–	123.3 ± 48.0	145.2 ± 43.6	191.0 ± 39.4	202.2 ± 34.9	–	181.1 ± 35.5	229.3 ± 33.5	298.3 ± 31.4	268.4 ± 28.8

Source IRAS	155 MHz (mJy)	158 MHz (mJy)	166 MHz (mJy)	174 MHz (mJy)	181 MHz (mJy)	189 MHz (mJy)	197 MHz (mJy)	200 MHz (mJy)	204 MHz (mJy)	212 MHz (mJy)	220 MHz (mJy)	227 MHz (mJy)
F00198-7926	–	149.7 ± 38.3	68.6 ± 34.1	188.8 ± 42.2	135.1 ± 40.5	81.0 ± 36.9	156.3 ± 39.2	–	108.2 ± 38.5	114.5 ± 40.4	137.0 ± 41.5	–
F00199-7426	67.5 ± 19.1	–	–	–	–	–	–	37.4 ± 12.0	–	–	–	–
F01268-5436	–	118.6 ± 23.8	65.8 ± 22.0	88.1 ± 22.7	79.0 ± 22.2	102.9 ± 22.0	85.1 ± 23.1	–	97.4 ± 19.1	51.6 ± 18.2	58.5 ± 18.0	86.6 ± 19.6
F01388-4618	20.1 ± 7.4	–	–	–	–	–	–	25.6 ± 5.7	–	–	–	–
F01419-6826	9.8 ± 9.8	–	–	–	–	–	–	19.3 ± 19.3	–	–	–	–
F02364-4751	–	58.5 ± 13.8	52.8 ± 13.2	61.2 ± 14.7	27.0 ± 12.2	57.5 ± 12.7	61.1 ± 12.6	–	40.9 ± 14.5	21.7 ± 12.8	61.7 ± 13.7	29.1 ± 13.6
F03068-5346	–	104.2 ± 18.4	107.4 ± 18.6	91.7 ± 17.9	74.0 ± 15.7	96.7 ± 16.5	77.0 ± 16.7	–	74.3 ± 14.3	74.3 ± 14.4	49.7 ± 12.3	62.7 ± 13.0
F03481-4012	–	40.1 ± 21.2	59.4 ± 20.2	25.2 ± 20.4	84.4 ± 21.4	91.4 ± 21.4	70.6 ± 19.4	–	57.0 ± 15.1	70.3 ± 15.2	62.2 ± 15.1	82.3 ± 15.6
F04063-3236	–	22.3 ± 18.0	40.8 ± 16.2	3.1 ± 15.5	31.0 ± 13.3	15.8 ± 12.9	40.5 ± 12.2	–	47.0 ± 14.2	10.4 ± 12.5	47.9 ± 13.3	58.2 ± 14.1
F06021-4509	48.8 ± 14.2	–	–	–	–	–	–	7.4 ± 7.4	–	–	–	–
F06035-7102	–	483.9 ± 54.9	480.6 ± 55.2	534.6 ± 60.5	458.3 ± 54.4	465.5 ± 54.6	375.6 ± 48.2	–	436.4 ± 52.7	412.5 ± 49.9	366.9 ± 45.4	408.6 ± 49.9
F06206-6315	30.8 ± 8.8	–	–	–	–	–	–	23.5 ± 8.4	–	–	–	–
F18582-5558	21.9 ± 21.9	–	–	–	–	–	–	12.6 ± 12.6	–	–	–	–
F20117-3249	22.2 ± 22.2	–	–	–	–	–	–	86.5 ± 15.4	–	–	–	–
F20445-6218	16.8 ± 16.8	–	–	–	–	–	–	15.6 ± 15.6	–	–	–	–
F21178-6349	14.2 ± 14.2	–	–	–	–	–	–	13.0 ± 13.0	–	–	–	–
F21292-4953	–	78.2 ± 17.4	47.9 ± 14.8	23.0 ± 15.3	55.5 ± 16.2	24.0 ± 15.2	82.0 ± 16.7	–	72.7 ± 17.4	43.9 ± 17.9	28.6 ± 16.6	49.5 ± 17.3
F21295-4634	10.5 ± 10.5	–	–	–	–	–	–	21.7 ± 8.0	–	–	–	–
F23389-6139	–	239.4 ± 27.4	273.0 ± 27.5	239.8 ± 26.3	286.6 ± 31.7	317.2 ± 30.7	292.4 ± 29.5	–	272.5 ± 29.2	250.0 ± 27.6	269.6 ± 26.6	255.5 ± 26.8

Table A2. An overview of all flux density measurements, obtained from the literature, that were used for sources in our samples. '-' denote sources without a measurement for that survey or instrument. References: SUMSS – Mauch et al. (2013), NVSS – Condon et al. (1998), PMN – Gregory et al. (1994), IRAS – Moshir (1990), AKARI – Yamamura et al. (2010), ISOPHOT – Klaas et al. (2001).

Source	SUMSS	NVSS	PMN	IRAS		AKARI			ISOPHOT					
IRAS	843 MHz (mJy)	1.4 GHz (mJy)	4.85 GHz (mJy)	3000 GHz (Jy)	5000 GHz (Jy)	2141 GHz (Jy)	3330 GHz (Jy)	4160 GHz (Jy)	1470 GHz (Jy)	1620 GHz (Jy)	1860 GHz (Jy)	2520 GHz (Jy)	3150 GHz (Jy)	4930 GHz (Jy)
F00198-7926	36.7 ± 3.0	-	-	2.9 ± 0.3	3.1 ± 0.2	-	2.4 ± 0.2	-	-	-	-	-	-	-
F00199-7426	40.8 ± 3.6	-	-	6.4 ± 0.5	4.2 ± 0.3	5.4 ± 0.5	4.4 ± 0.3	3.9 ± 0.3	3.0 ± 0.9	4.2 ± 1.3	5.3 ± 1.6	7.5 ± 2.3	-	-
F01268-5436	20.3 ± 1.6	-	-	2.3 ± 0.2	1.7 ± 0.2	2.5 ± 0.5	1.6 ± 0.1	-	-	-	-	-	-	-
F01388-4618	19.7 ± 1.4	-	-	3.7 ± 0.3	2.9 ± 0.3	-	2.8 ± 0.2	-	-	-	-	-	-	-
F01419-6826	12.5 ± 1.1	-	-	2.5 ± 0.2	2.2 ± 0.1	-	2.8 ± 0.2	-	-	-	-	-	-	-
F02364-4751	29.7 ± 1.9	-	-	5.0 ± 0.4	2.8 ± 0.2	4.0 ± 0.5	3.2 ± 0.2	-	-	-	-	-	-	-
F03068-5346	28.9 ± 2.2	-	-	4.0 ± 0.3	3.4 ± 0.2	-	2.9 ± 0.2	3.1 ± 0.3	1.4 ± 0.4	1.7 ± 0.5	-	-	-	-
F03481-4012	21.9 ± 1.7	15.8 ± 1.1	-	2.6 ± 0.2	1.8 ± 0.1	-	1.6 ± 0.1	-	-	-	-	-	-	-
F04063-3236	11.9 ± 1.6	11.5 ± 1.2	-	2.1 ± 0.2	1.8 ± 0.1	-	1.7 ± 0.2	-	-	-	-	-	-	-
F06021-4509	10.9 ± 1.3	-	-	2.4 ± 0.3	1.6 ± 0.1	-	1.4 ± 0.1	-	-	-	-	-	-	-
F06035-7102	152.0 ± 10.7	-	-	5.7 ± 0.4	5.1 ± 0.3	4.8 ± 0.3	4.5 ± 0.2	4.6 ± 0.3	1.4 ± 0.4	2.0 ± 0.6	2.9 ± 0.9	5.2 ± 1.6	5.0 ± 1.5	5.9 ± 1.8
F06206-6315	22.6 ± 1.6	-	-	4.6 ± 0.4	4.0 ± 0.2	4.0 ± 0.3	3.5 ± 0.2	3.5 ± 0.3	1.5 ± 0.5	1.9 ± 0.6	2.9 ± 0.9	4.6 ± 1.4	4.2 ± 1.3	4.8 ± 1.5
F18582-5558	12.0 ± 1.2	-	-	-	1.9 ± 0.2	-	1.8 ± 0.1	-	-	-	-	-	-	-
F20117-3249	54.4 ± 3.5	57.1 ± 3.4	-	-	1.5 ± 0.1	-	2.3 ± 0.2	-	-	-	-	-	-	-
F20445-6218	17.8 ± 1.4	-	-	2.9 ± 0.3	2.2 ± 0.1	2.9 ± 0.4	2.1 ± 0.2	-	-	-	-	-	-	-
F21178-6349	10.2 ± 1.4	-	-	2.0 ± 0.2	1.6 ± 0.1	-	1.4 ± 0.1	-	-	-	-	-	-	-
F21292-4953	28.5 ± 1.9	-	-	3.1 ± 0.3	2.5 ± 0.2	3.5 ± 0.6	2.5 ± 0.2	-	-	-	-	-	-	-
F21295-4634	18.2 ± 1.4	-	-	3.2 ± 0.3	2.4 ± 0.2	-	-	-	-	-	-	-	-	-
F23389-6139	166.0 ± 9.7	-	59.0 ± 8.5	4.3 ± 0.3	3.6 ± 0.2	-	-	-	1.5 ± 0.5	2.0 ± 0.6	2.8 ± 0.9	4.0 ± 1.2	3.3 ± 1.0	3.9 ± 1.2

Table A3. An overview of all radio-continuum flux density measurements produced using ATCA data obtained under the project code C2993 as part of this study. '-' denote sources without a measurement for that central frequency.

Source	1.5 GHz	1.6 GHz	1.8 GHz	2.0 GHz	2.2 GHz	2.4 GHz	2.6 GHz	2.8 GHz	4.4 GHz	4.5 GHz	5.0 GHz	5.5 GHz (This Study)	5.6 GHz	6.3 GHz	6.8 GHz	7.2 GHz	7.3 GHz	8.3 GHz	8.8 GHz	9.2 GHz	17.0 GHz	21.0 GHz	43.1 GHz	48.1 GHz
IRAS	(mJy)	(mJy)	(mJy)	(mJy)	(mJy)	(mJy)	(mJy)	(mJy)	(mJy)	(mJy)	(mJy)	(mJy)	(mJy)	(mJy)	(mJy)	(mJy)	(mJy)	(mJy)	(mJy)	(mJy)	(mJy)	(mJy)	(mJy)	(mJy)
F00198-7926	19.4 ± 1.2	-	-	14.9 ± 1.0	-	12.3 ± 0.9	-	11.0 ± 0.9	10.4 ± 0.7	-	9.7 ± 0.6	-	8.9 ± 0.6	8.0 ± 0.6	-	-	6.7 ± 0.5	-	5.7 ± 0.4	-	3.5 ± 0.3	2.7 ± 0.3	1.5 ± 0.2	1.4 ± 0.3
F00199-7426	19.0 ± 1.2	-	-	16.9 ± 1.1	-	14.3 ± 0.9	-	13.3 ± 0.9	10.7 ± 0.7	-	9.9 ± 0.6	-	8.6 ± 0.6	7.8 ± 0.6	-	-	6.6 ± 0.5	-	5.0 ± 0.4	-	3.4 ± 0.2	2.5 ± 0.3	1.5 ± 0.2	2.0 ± 0.3
F01268-5436	10.2 ± 0.8	-	-	8.4 ± 0.7	-	7.4 ± 0.7	-	7.2 ± 0.6	5.0 ± 0.4	-	4.2 ± 0.4	-	3.5 ± 0.4	3.4 ± 0.3	-	-	2.9 ± 0.2	-	1.9 ± 0.3	-	1.8 ± 0.2	1.4 ± 0.3	1.0 ± 0.1	1.1 ± 0.2
F01388-4618	9.2 ± 0.8	-	-	8.3 ± 0.7	-	8.4 ± 0.7	-	7.8 ± 0.6	6.4 ± 0.4	-	5.9 ± 0.4	-	5.5 ± 0.4	4.6 ± 0.3	-	-	4.0 ± 0.3	-	3.2 ± 0.3	-	2.0 ± 0.2	1.8 ± 0.3	0.9 ± 0.1	1.2 ± 0.2
F01419-6826	7.0 ± 0.6	-	-	7.0 ± 0.5	-	6.6 ± 0.6	-	4.8 ± 0.7	4.2 ± 0.3	-	3.6 ± 0.3	-	3.1 ± 0.3	2.9 ± 0.2	-	-	2.7 ± 0.2	-	2.2 ± 0.2	-	1.6 ± 0.2	1.0 ± 0.2	-	1.3 ± 0.3
F02364-4751	17.5 ± 1.1	-	-	14.0 ± 0.9	-	12.1 ± 0.8	-	12.2 ± 0.8	8.9 ± 0.5	-	7.3 ± 0.4	-	6.8 ± 0.4	5.8 ± 0.4	-	-	5.2 ± 0.4	-	3.6 ± 0.4	-	2.9 ± 0.2	2.2 ± 0.2	1.4 ± 0.1	1.2 ± 0.2
F03068-5346	-	-	9.5 ± 1.0	-	-	-	6.0 ± 0.9	-	6.9 ± 0.6	-	6.4 ± 0.8	-	6.0 ± 0.7	5.4 ± 0.6	-	-	4.4 ± 0.6	-	4.4 ± 0.3	-	3.6 ± 0.4	2.7 ± 0.3	1.7 ± 0.1	2.0 ± 0.2
F03481-4012	11.3 ± 0.7	-	-	10.5 ± 0.6	-	8.7 ± 0.6	-	8.3 ± 0.6	5.9 ± 0.4	-	6.1 ± 0.4	-	5.3 ± 0.4	4.8 ± 0.3	-	-	3.8 ± 0.3	-	3.0 ± 0.3	-	2.2 ± 0.2	1.8 ± 0.3	0.9 ± 0.1	0.7 ± 0.2
F04063-3236	7.4 ± 0.5	-	-	6.5 ± 0.5	-	5.5 ± 0.5	-	5.8 ± 0.6	4.8 ± 0.4	-	5.5 ± 0.3	-	4.8 ± 0.3	5.0 ± 0.3	-	-	3.9 ± 0.3	-	2.9 ± 0.3	-	1.8 ± 0.2	1.3 ± 0.3	0.8 ± 0.1	-
F06021-4509	7.1 ± 0.6	-	-	7.5 ± 0.6	-	6.8 ± 0.6	-	5.8 ± 0.6	4.8 ± 0.3	-	4.8 ± 0.3	-	4.4 ± 0.3	4.2 ± 0.2	-	-	3.6 ± 0.2	-	3.0 ± 0.2	-	1.7 ± 0.2	1.1 ± 0.2	1.2 ± 0.2	1.3 ± 0.3
F06035-7102	-	-	-	-	-	-	-	-	20.6 ± 2.8	-	20.1 ± 2.6	-	17.8 ± 2.2	16.1 ± 2.0	-	-	13.4 ± 1.6	-	11.0 ± 1.2	-	7.0 ± 2.2	5.1 ± 2.3	1.8 ± 0.2	2.0 ± 0.3
F06206-6315	15.5 ± 0.9	-	-	14.6 ± 0.9	-	14.7 ± 0.9	-	13.2 ± 0.8	11.4 ± 0.6	-	10.5 ± 0.6	-	9.4 ± 0.5	8.8 ± 0.5	-	-	7.7 ± 0.4	-	6.6 ± 0.4	-	3.5 ± 0.4	2.8 ± 0.3	1.5 ± 0.2	2.3 ± 0.3
F18582-5558	6.7 ± 0.6	-	-	7.1 ± 0.6	-	7.0 ± 0.6	-	7.4 ± 0.6	6.0 ± 0.5	-	5.8 ± 0.5	-	5.5 ± 0.5	5.0 ± 0.5	-	4.8 ± 0.5	-	4.3 ± 0.4	-	3.9 ± 0.3	-	2.0 ± 0.3	0.8 ± 0.1	-
F20117-3249	49.7 ± 2.5	-	-	44.7 ± 2.3	-	41.2 ± 2.2	-	36.8 ± 2.0	25.4 ± 1.7	-	23.4 ± 1.7	-	19.2 ± 1.6	16.2 ± 1.4	-	-	13.0 ± 1.4	-	9.8 ± 1.1	-	7.1 ± 0.6	5.1 ± 0.6	2.9 ± 0.1	2.3 ± 0.2
F20445-6218	9.0 ± 0.6	-	-	8.2 ± 0.6	-	7.1 ± 0.5	-	6.0 ± 0.5	4.7 ± 0.4	-	3.8 ± 0.4	-	3.5 ± 0.4	3.2 ± 0.3	-	-	2.8 ± 0.3	-	2.4 ± 0.3	-	1.7 ± 0.2	1.4 ± 0.2	0.9 ± 0.1	-
F21178-6349	-	5.1 ± 0.5	-	-	4.0 ± 0.4	-	-	2.8 ± 0.5	-	2.2 ± 0.2	-	1.6 ± 0.2	-	-	1.6 ± 0.2	-	-	-	-	-	1.1 ± 0.1	0.8 ± 0.3	-	-
F21292-4953	-	-	16.6 ± 1.8	-	-	-	-	-	-	-	-	9.7 ± 1.0	-	-	8.0 ± 0.9	-	-	-	7.5 ± 0.9	-	6.4 ± 0.6	4.4 ± 0.7	-	-
F21295-4634	10.1 ± 0.8	-	-	10.2 ± 0.8	-	7.5 ± 0.8	-	4.4 ± 0.7	3.7 ± 0.5	-	4.1 ± 0.5	-	3.2 ± 0.5	3.0 ± 0.5	-	-	2.3 ± 0.4	-	1.9 ± 0.3	-	1.8 ± 0.2	1.1 ± 0.3	0.5 ± 0.1	-
F23389-6139	117.8 ± 6.0	-	-	100.4 ± 5.1	-	91.3 ± 4.7	-	82.3 ± 4.3	56.1 ± 0.8	-	49.2 ± 0.9	-	41.8 ± 0.9	37.1 ± 0.9	-	28.2 ± 1.0	-	-	25.0 ± 0.6	-	10.4 ± 0.3	8.3 ± 0.6	3.9 ± 0.2	3.8 ± 0.3

APPENDIX B: SPECTRAL ENERGY DISTRIBUTIONS

In this section, we present all SEDs, with the most supported model overlaid, for each source. All available flux density measurements have been included (Fig. B1).
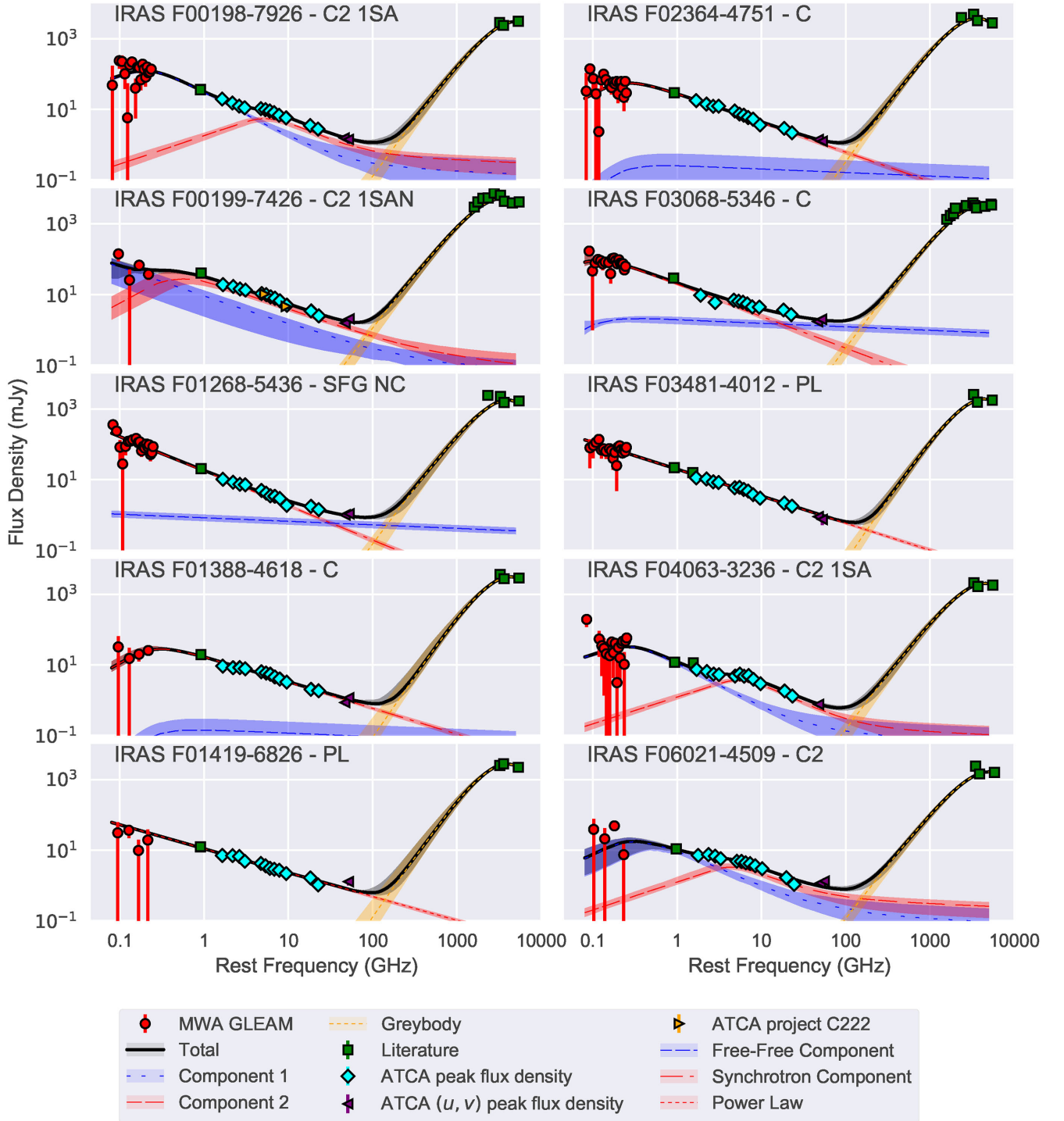
Figure B1. The observed data and preferred SED modelling of the SFGs from our sample in RA order. We include any components that make up the most preferred model focusing on the radio continuum. Highlighted regions represent the 1σ uncertainty sampled by EMCEE.
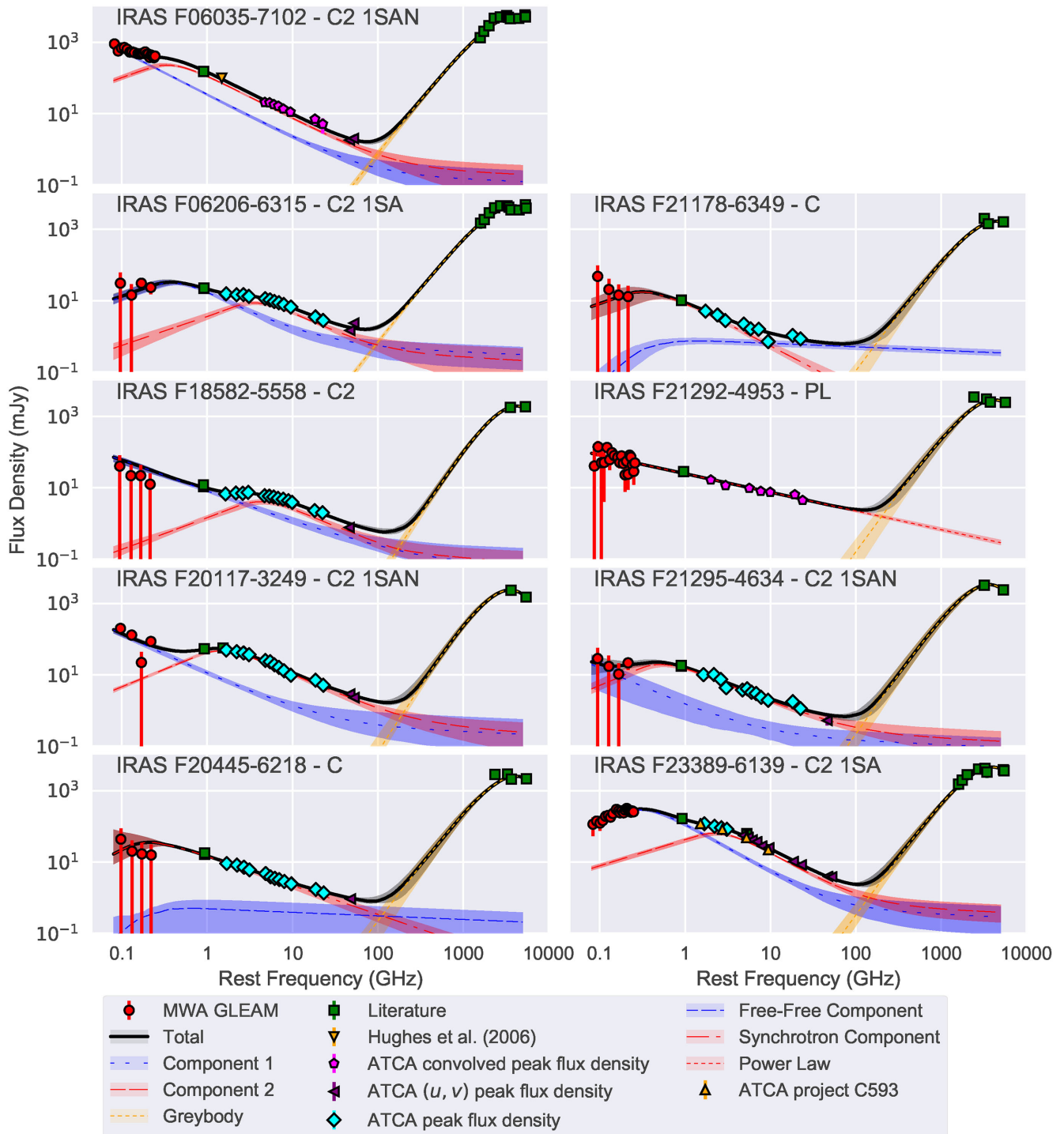
Figure B1 – *Continued*

[1]*University of Western Sydney, Locked Bag 1797, Penrith, NSW 2751, Australia*

[2]*International Centre for Radio Astronomy Research, Curtin University, Bentley, WA 6102, Australia*

[3]*CSIRO Astronomy and Space Science, Marsfield, NSW 1710, Australia*

[4]*Department of Physics and Astronomy, Macquarie University, Sydney, NSW 2109, Australia*

[5]*Australian Gemini Office, Australian Astronomical Observatory, PO Box 915, Sydney, NSW 1670, Australia*

[6]*ARC Centre of Excellence for All-Sky Astrophysics (CAASTRO), Bentley, WA 6102, Australia*

[7]*Sydney Institute for Astronomy, School of Physics, The University of Sydney, NSW 2006, Australia*

[8]*International Centre for Radio Astronomy Research, University of Western Australia, Crawley 6009, Australia*

[9]*Raman Research Institute, Bangalore 560080, India*

[10]*Dunlap Institute for Astronomy and Astrophysics, 50 St. George St, University of Toronto, ON M5S 3H4, Canada*

[11]*School of Chemical & Physical Sciences, Victoria University of Wellington, Wellington 6140, New Zealand*
[12]*Peripety Scientific Ltd., PO Box 11355 Manners Street, Wellington 6142, New Zealand*
[13]*Research School of Astronomy and Astrophysics, Australian National University, Canberra, ACT 2611, Australia*

[14]*Netherlands Institute for Radio Astronomy (ASTRON), PO Box 2, NL-7990 AA Dwingeloo, the Netherlands*
[15]*School of Physics, The University of Melbourne, Parkville, VIC 3010, Australia*

This paper has been typeset from a TeX/LaTeX file prepared by the author.